Restoring the continuum limit in the time-dependent numerical renormalization group approach

Jan Böker and Frithjof B. Anders
Lehrstuhl für Theoretische Physik II, Technische Universität Dortmund Otto-Hahn-Str. 4, 44227 Dortmund, Germany

(Received 14 June 2020; revised 17 August 2020; accepted 18 August 2020; published 31 August 2020)

The continuous coupling function in quantum impurity problems is exactly partitioned into a part represented by a finite-size Wilson chain and a part represented by a set of additional reservoirs, each coupled to one Wilson chain site. These additional reservoirs represent high-energy modes of the environment neglected by the numerical renormalization group and are required to restore the continuum limit of the original problem. We present a hybrid time-dependent numerical renormalization group approach which combines an accurate numerical renormalization group treatment of the nonequilibrium dynamics on the finite-size Wilson chain with a Bloch-Redfield formalism to include the effect of these additional reservoirs. Our approach overcomes the intrinsic shortcoming of the time-dependent numerical renormalization group approach induced by the bath discretization with a Wilson parameter $\Lambda > 1$. We analytically prove that for a system with a single chemical potential, the thermal equilibrium reduced density operator is the steady-state solution of the Bloch-Redfield master equation. For the numerical solution of this master equation, a Lanczos method is employed which couples all energy shells of the numerical renormalization group. The presented hybrid approach is applied to the real-time dynamics in correlated fermionic QISs. An analytical solution of the resonant-level model serves as a benchmark for the accuracy of the method which is then applied to nontrivial models, such as the interacting resonant-level model and the single-impurity Anderson model.

DOI: 10.1103/PhysRevB.102.075149

I. INTRODUCTION

Quantum impurity systems (QISs) have been of increasing interest in the last two decades due to the advent of single-electron transistors [1] and the observation of the Kondo effect in nanodevices [2–4] as well as in adatoms [5,6] and molecules [7] on surfaces. Charge and spin dynamics of molecules on surfaces [8,9], including inelastic processes [10–12] as well as local moment formations and quantum phase transitions in the vicinity of graphene vacancies [13–16], are only a few examples of many such different realizations. QISs are also of fundamental importance as a part of the dynamical mean field theory [17,18] where a correlated lattice problem is mapped onto an effective QIS [19] augmented by a self-consistence condition.

On the route to functional nanodevices, the real-time dynamics of local charge [20] or spin degrees of freedom (DOF) [21] sparked theoretical interest in nonequilibrium dynamics of observables in such systems [22,23]. Charge-transfer and energy-transfer dynamics in molecular systems have also been investigated for more than two decades [24].

The theoretical approaches addressing nonequilibrium dynamics can be divided into three categories. The first class of approaches relies on partitioning the full continuum Hamiltonian into an exactly solvable part and a residue treated as a perturbation. Amongst those are the Keldysh diagrammatic approaches [25–27] to quantum impurity problems [28,29] as well as more advanced functional renormalization group [30,31], real-time renormalization group [32], and flow equation methods [33,34]. The extension of diagrammatic quantum Monte Carlo methods [35] to the real-time dynamics suffers from a sign problem [36–38] which has been tamed by the worm inch algorithm [39] only recently. The second class of approaches replaces the closed continuum problem by a finite-size representation of relevant impurity DOF subject to a Lindblad or Bloch-Redfield master equation [24,40]. Such approaches have been proposed for systems that are coupled only weakly to their environment but also have been extended to more complex QIS [41,42] targeting quantum transport problems out of equilibrium. The latter extension uses the Lindblad decay rates as fitting parameters to reproduce the continuum limit of the noninteracting part of the original problem as accurately as possible. The third class of methods performs a mapping of the original continuum problem onto a discretized representation which is then treated by exact diagonalization [43,44], pure state propagation [45–49] by the time-dependent numerical renormalization group (TD-NRG) [50–54], or the time-dependent density matrix renormalization group (TD-DMRG) approach [55–57].

In this paper, we propose a hybrid TD-NRG approach that combines the virtue of the NRG [50,51,58] encoding an accurate representation of equilibrium fixed points with a Bloch-Redfield master equation approach [24] to restore the original continuum problem. In the previous hybrid TD-NRG algorithms, different numerical methods (TD-NRG and Chebyshev polynomials [59] or TD-NRG and TD-DMRG [60]) were combined but still operated on a finite one-dimensional chain representation of the Hamiltonian and did not solve the fundamental limitation of all finite-size representations: true relaxation and thermalization. In a chain

representation of the problem, the continuity equations derived from charge conservation lead to back reflections within the Wilson chain [59] or at the end of a tight-binding chain [61].

We make use of the exact decomposition of the bath continuum into the Wilson chain and augmented reservoirs attached to each chain site. We adopt the proposal [62] made in the context of the spin-boson model [22] to fermionic baths. In the previous work [62], only corrections to the Wilson chain parameters obtained from the real part of the bosonic reservoir coupling function were included in the calculations for the spin-boson model [63]. Here, we link the Bloch-Redfield tensor [24] to the previously neglected imaginary parts of the fermionic reservoir correlation functions: These tensor elements govern the real-time dynamics of the reduced density matrix by connecting NRG eigenstates on different Wilson shells [50,51,58] or NRG iterations. In our algorithm, the static reduced density matrix in the TD-NRG [50,51] is replaced by a time-dependent version and its dynamics is generated by the previously neglected reservoirs. Our approach conserves the trace of the density matrix at any time and approaches thermal equilibrium as the steady-state solution for any Bloch-Redfield tensor that fulfills the generic detailed balance condition. Therefore, our approach corrects the drawback of all finite-size real-time methods, namely, that a true stationary steady state can only be reached in the limit of an infinite system size that is not accessible for such methods.

The paper is organized as follows. In Sec. II, we introduce the generic quantum impurity model and derive the exact hybrid Wilson-chain continuum representation of the original coupling function in Sec. II C. In Sec. II D, we show that the resulting reservoir coupling functions approach two alternating fixed points: one for the even chain sites and one for the odd chain sites that is typical for fermionic baths [64,65]. The proposed hybrid approach is presented in Sec. III. After a short review of the TD-NRG to introduce the notation, we derive the effect of the additional reservoirs up to second order in the fermionic coupling functions in Sec. III B which are used in Sec. III C to obtain the nonequilibrium dynamics of the reduced density matrix providing the essential of the hybrid approach. Some technical details about the implementation are provided in Sec. III D. In Sec. IV, we present the benchmark for our approach by demonstrating excellent agreement between the predictions of the continuum hybrid TD-NRG approach and the exact analytic solution of the charge dynamics in the resonant-level model (RLM) [51]. The nonequilibrium dynamics of two correlated models, the interacting RLM [66,67], and the single-impurity Anderson model (SIAM) [65] are discussed, and the paper ends with a short summary.

II. DISCRETIZATION AND RESTORING OF THE CONTINUUM LIMIT

A. Introduction to quantum impurity models

Quantum impurity models (QISs) describe the coupling of a strongly interacting quantum impurity $H_{\rm imp}$ with noninteracting baths $H_{\rm bath}$ comprising either conduction bands [64,65] or a bosonic environment [22]:

$$H = H_{\rm imp} + H_{\rm bath} + H_I. \tag{1}$$

The term H_I describes the interaction between the two subsystems. $H_{\rm bath}$ models M different noninteracting and continuous fermionic baths,

$$H_{\rm bath} = \sum_{\nu=1}^{M} \sum_{k} \epsilon_{k\nu} c_{k\nu}^\dagger c_{k\nu}, \tag{2}$$

with the flavors ν. $c_{k\nu}^\dagger$ creates a bath electron of flavor ν with the energy $\epsilon_{k\nu}$. ν might label the spin σ or the channel α in multiband models. We focus on a coupling H_I between the two subsystems described by a single particle hybridization,

$$H_I = \sum_{\nu=1}^{M} V_\nu (c_{0\nu}^\dagger A_\nu + A_\nu^\dagger c_{0\nu}), \tag{3}$$

where $c_{0\nu}$ annihilates a local bath state of flavor ν defined as a linear combination of annihilators $c_{k\nu}$ of bath modes with the eigenenergy $\epsilon_{k\nu}$,

$$c_{0\nu} = \sum_{k} \lambda_{k\nu} c_{k\nu}, \tag{4}$$

such that $c_{0\nu}$ fulfils canonical commutation relations. $A_\nu^\dagger (A_\nu)$ accounts for the linear combination of local orbital creation (annihilation) operators inducing transitions in the impurity that change the particle number by one. The coupling parameters $\lambda_{k\nu}$ contain the possible energy-dependent hybridization.

By integrating out the bath DOF in a path integral formulation of the partition function, it was noted early on [22,64,68] that the influence of the bath onto the local impurity dynamics is fully determined by the coupling function $\Delta_\nu(z)$ defined as

$$\Delta_\nu(z) = V_\nu^2 \sum_{k} \frac{\lambda_{k\nu}^2}{z - \epsilon_{k\nu}}. \tag{5}$$

We will utilize the fact that different types of reservoirs [68] yield the same local dynamics as long as they provide the identical coupling functions $\Delta_\nu(z)$. The spectral function

$$\Gamma_\nu(\omega) = \lim_{\delta \to 0^+} {\rm Im}\Delta_\nu(\omega - i\delta) \tag{6}$$

determines the influence of the νth bath onto the local dynamics. For nonsymmetric baths [22], the real part ${\rm Re}\Delta_\nu(\omega)$ causes an additional energy renormalization of impurity eigenenergies. This energy renormalization strongly influences the dynamics close to a local quantum critical point [62,69,70] in the case of bosonic baths but plays a less pronounced role in fermionic baths.

B. Discretization of the continuum model

The NRG [58,64] is one of the powerful methods developed to accurately solve QIS. Within this approach, the bath continuum is discretized on a logarithmic mesh controlled by the parameter $\Lambda > 1$. The Hamiltonian is then mapped onto a semi-infinite chain,

$$H^{\rm NRG} = \lim_{N \to \infty} H_N^{\rm NRG}, \tag{7}$$

$$H_N^{\rm NRG} = H_{\rm imp} + H_{I-C} + H_{\rm chain}(N), \tag{8}$$

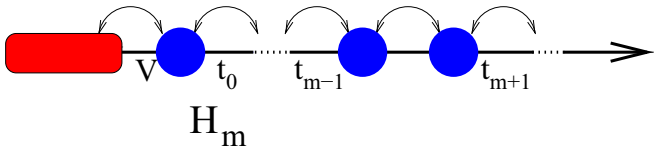

FIG. 1. The semi-infinite Wilson chain depicted up to the chain link m.

$$H_{\text{chain}}(N) = \sum_{m=0}^{N}\sum_{\nu=1}^{M}\epsilon_{m\nu}f_{m\nu}^{\dagger}f_{m\nu} + \sum_{m=1}^{N}\sum_{\nu=1}^{M}t_{m-1\nu}(f_{m\nu}^{\dagger}f_{m-1\nu} + f_{m-1\nu}^{\dagger}f_{m\nu}),$$
$$H_{I-C} = \sum_{\nu=1}^{M}V_{\nu}(f_{0\nu}^{\dagger}A_{\nu} + A_{\nu}^{\dagger}f_{0\nu}), \tag{9}$$

whose chain topology is depicted in Fig. 1. The mth chain site represents an exponentially decreasing energy scale $\omega_m = D\Lambda^{-(m-1)/2}(1+\Lambda^{-1})/2$, and the original Hamiltonian is only restored [64] in the limit $\Lambda \to 1^+$. The tight-binding parameters t_m also decrease exponentially, $t_m \propto \Lambda^{-m/2}$, which establishes the hierarchy of scales in the sequence of finite-size Hamiltonians H_m^{NRG}. The bath asymmetry [58] mentioned above enters the single particle energies $\epsilon_{m\nu}$ of each chain site.

This sequence of H_m^{NRG} is iteratively diagonalized, discarding the high-energy states at each step to maintain a manageable number of states. Thereby, the set of eigenstates of H_m^{NRG}, $\{|r,e;m\rangle\}$, with the corresponding eigenenergies E_r^m is partitioned into a set of kept (k) states $S_k = \{|k,e;m\rangle\}$ and a set of states $S_d = \{|l,e;m\rangle\}$ which will be discarded (d) in the next NRG iteration. Since the iteration is stopped at a finite but arbitrary value $m = N$, we have augmented the eigenstate $|k\rangle$ at iteration m with the configuration e of the decoupled rest chain $m+1 \to N$ to obtain a complete basis set—for details see Refs. [50,51]. The reduced basis set of H_m^{NRG}, S_k, thus obtained is expected to faithfully describe the spectrum of the full Hamiltonian on the scale of D_m, corresponding [64] to a temperature $T_m \sim D_m$ from which all thermodynamic expectation values are calculated. The NRG algorithm is stopped at chain length N when the lowest temperature of interest is reached.

In the present paper, we will not discuss the explicit construction of such chains as a faithful representation of the original continuous baths and refer the reader to the reviews [56,58,64] on this subject. Here we assume that the NRG framework has already provided us with all chain parameters such as nearest-neighbor hopping $t_{m\nu}$ and orbital energy $\epsilon_{m\nu}$ of each chain link to fully characterize any chain depicted in Fig. 1.

Independently of whether the NRG approach, exact diagonalization, or the density matrix renormalization group (DMRG) [56,71] is used to solve such a finite-size representation of an interacting QIS, these numerical approaches suffer from the same fundamental problem: The finite-size chain Hamiltonian does not contain any information on the lifetime of excitations and lacks the mechanism for a locally excited system to relax into the true thermodynamic ground state.

This leads to two severe limitations when calculating the spectral functions within the NRG: (i) details at high energies are lost by overbroadening ($b_m \propto D_m$), even if the peak position and its spectral weight are calculated correctly within the method, and (ii) spectral information for frequencies below the smallest energy scale, i.e., $|\omega| < D_N$, is absent, which limits the accuracy of the NRG for calculating transport properties [58,72,73].

C. Restoring the continuum limit

We adapt the approach [62] introduced in the context of the spin-boson model [22] to fermionic baths to reconstruct the correct hybridization function $\Delta_\nu(z)$ for a given Wilson chain. We will drop the flavor index ν and restrict ourselves to a single flavor for simplicity. We will restore the flavor index of the bath modes at the end of this section.

Since the influence of the continuous bath onto the local dynamics of the quantum impurity is fully determined by the function $\Delta(z)$, the bath Hamiltonian $\tilde{H}_{\text{bath}}(1)$ defined as

$$\tilde{H}_{\text{bath}}(1) = \epsilon_0 f_0^{\dagger}f_0 + \sum_k \epsilon_{k0}c_{k0}^{\dagger}c_{k0} + V_0(f_0^{\dagger}c_{00} + c_{00}^{\dagger}f_0) \tag{10}$$

yields the same local dynamics as the original H_{bath} if the Green's function (GF) of the original bath $G_{c_0;c_0^{\dagger}}(z)$ is identical to the GF $G_{f_0;f_0^{\dagger}}(z)$,

$$\Delta(z) = V^2 G_{c_0;c_0^{\dagger}}(z) = V^2 G_{f_0;f_0^{\dagger}}(z), \tag{11}$$

and the hybridization in Eq. (3) is replaced by

$$H_I = V(f_0^{\dagger}A + A^{\dagger}f_0). \tag{12}$$

The index 1 in $\tilde{H}_{\text{bath}}(1)$ indicates that H_{bath} has been replaced by a new bath coupled to a single auxiliary orbital. This new degree of freedom, f_0, will become the first site of the chain representation of the bath continuum which we will construct in the following. Analog to Eq. (4), we have defined the new operator c_{00} of the new reservoir 0,

$$c_{00} = \sum_k \lambda_{k0}c_{k0}, \quad \sum_k \lambda_{k0}^2 = 1 \tag{13}$$

as a linear combination of its reservoir modes.

The bath Hamiltonian Eq. (10) describes a RLM whose GF $G_{f_0;f_0^{\dagger}}(z)$ is given by

$$G_{f_0;f_0^{\dagger}}(z) = \frac{1}{z - \epsilon_0 - V_0^2 G_{c_{00};c_{00}^{\dagger}}(z)}. \tag{14}$$

The unknown reservoir coupling function $\Delta_0(z)$, defined as

$$\Delta_0(z) \equiv V_0^2 G_{c_{00};c_{00}^{\dagger}}(z), \tag{15}$$

is simply related to $\Delta(z)$ via Eq. (11):

$$\Delta_0(z) = z - \epsilon_0 - \frac{1}{G_{f_0;f_0^{\dagger}}(z)} = z - \epsilon_0 - \frac{V^2}{\Delta(z)}. \tag{16}$$

Since the spectrum of $G_{c_{00};c_{00}^{\dagger}}(z)$ must be normalized to unity, the coupling constant V_0^2 cannot be chosen freely in the model

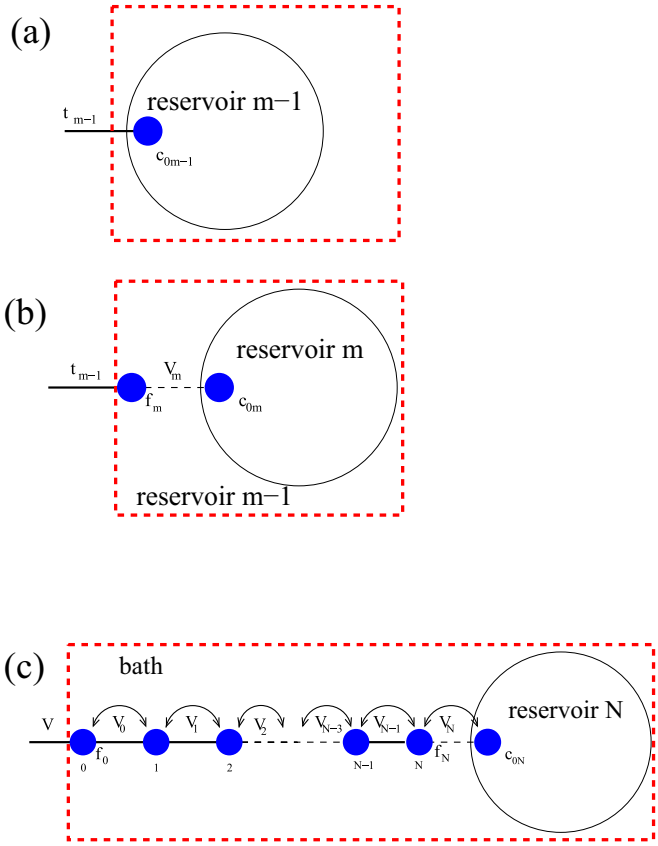

FIG. 2. The reservoir continuum $m-1$ (a) is recursively replaced by a single chain site f_m coupled to a new reservoir degree of freedom c_{0m} by a chain link matrix element V_m, shown in (b), to obtain a continuous fraction representation of the original bath by a (c) finite-size tight-binding chain with the continuous reservoir coupled to the end of the chain as used in DMRG calculations [74].

but is determined by the integral

$$\pi V_0^2 = \int_{-\infty}^{\infty} d\omega\, \mathrm{Im}\Delta_0(\omega - i\delta), \tag{17}$$

where ϵ_0 is given by the first momentum of the spectrum of $\Delta(z)$:

$$\epsilon_0 = \frac{1}{\pi V^2}\int_{-\infty}^{\infty} d\omega\, \omega\, \mathrm{Im}\Delta(\omega - i\delta). \tag{18}$$

Now we can apply the same arguments as above to the new reservoir $\Delta_0(z)$ and substitute it by another RLM comprising the second chain site of a chain coupled to the new reservoir 1. Recursively, we replace the previous reservoir $m-1$ at iteration m, shown in Fig. 2(a), by an effective RLM involving a new reservoir m as depicted in Fig. 2(b). After $N+1$ such steps, we obtain a chain of length $N+1$ which is coupled to a single reservoir N at the end, as plotted in Fig. 2(c).

The resulting chain parameters $\{V_m\}$ and $\{\epsilon_m\}$ represent a continuous fraction expansion with a finite length which has been successfully used in DMRG calculations [74]. The proper continuum limit is restored by adding a single additional reservoir coupled to the last chain site whose properties are uniquely determined by the original coupling function $\Delta(z)$. The tight-binding parameters V_m, however, always remain of the order of the original bandwidth D for all m in this procedure and Wilson chains with their refined built-in energy hierarchy cannot be generated this way.

To generate more general chains whose sites are coupled by arbitrary linking matrix elements t_m ($t_m < V_m$), we need to supplement the algorithm with another step at each iteration. We assume that at some iteration m the reservoir property is determined by a coupling function $\tilde{\Delta}_{m-1}(z)$ such that the corresponding GF is properly normalized by the coupling t_{m-1}^2:

$$G_{c_{0m-1};c_{0m-1}^\dagger}(z) = \frac{1}{t_{m-1}^2}\tilde{\Delta}_{m-1}(z). \tag{19}$$

We will explicitly specify $\tilde{\Delta}_{m-1}(z)$ below by showing how it is determined by the modified recursion. As before, we replace the reservoir $m-1$ by an additional chain site m coupled to a new reservoir m as depicted in Fig. 2(b). The new reservoir coupling function is obtained by the same recursion,

$$\Delta_m(z) = z - \tilde{\epsilon}_m - \frac{t_{m-1}^2}{\tilde{\Delta}_{m-1}(z)}, \tag{20}$$

where the total coupling matrix element is determined by the integral

$$V_m^2 = \frac{1}{\pi}\int_{-\infty}^{\infty} d\omega\, \mathrm{Im}\Delta_m(\omega - i\delta). \tag{21}$$

Since the new coupling function $\Delta_m(z)$ must be proportional to a GF, its real part must vanish for $|\omega| \to \infty$ as $1/\omega$. Therefore, the energy ϵ_m has to be calculated from the first momentum of $\tilde{\Delta}_{m-1}(z)$,

$$\tilde{\epsilon}_m = \frac{1}{\pi t_{m-1}^2}\int_{-\infty}^{\infty} d\omega\, \omega \mathrm{Im}\tilde{\Delta}_{m-1}(\omega - i\delta), \tag{22}$$

to correctly incorporate the center of mass of the previous reservoir. Although $\tilde{\epsilon}_m$ is of the same order as the original NRG Wilson chain parameter ϵ_m obtained by the standard NRG approach to a nonconstant density of states [58], we will show below that these values are not identical. To be consistent, we need to replace $\epsilon_m \to \tilde{\epsilon}_m$ as given by the first momentum Eq. (22). Therefore, we will only use the sets of $\{t_m\}$ from the NRG approach and replace the Wilson chain energies accordingly: $\epsilon_m \to \tilde{\epsilon}_m$.

Let us introduce a positive semidefinite but otherwise unspecified cutoff function $F_{d_m}(\omega)$ which is continuous, $0 \leqslant F_{d_m}(\omega) \leqslant 1$, and its smooth transition between 0 and 1 occurs on the energy scale d_m. For spectral functions $\Gamma_m(\omega) = \mathrm{Im}\Delta_m(w - i0^+)$ with nonzero contributions for positive and negative frequencies, which is the typical situation in the case of fermionic baths,[1] we demand

$$F_{d_m}(\omega) \to \begin{cases} 1 & \text{for } |\omega| \ll d_m \\ 0 & \text{for } |\omega| \gg d_m. \end{cases} \tag{23}$$

We use the cutoff function $F_{d_m}(\omega)$ to separate a high-energy part from a low-energy part of the coupling function $\Gamma_m(\omega)$,

$$\begin{aligned} \Gamma_m^L(\omega) &= F_{d_m}(\omega)\Gamma_m(\omega), \\ \Gamma_m^H(\omega) &= (1 - F_{d_m}(\omega))\Gamma_m(\omega), \end{aligned} \tag{24}$$

[1]For coupling functions which are nonzero only for $\omega > 0$, as is the case for bosonic baths [22], $F_{d_m}(\omega)$ must vanish for all $\omega < 0$ [62].

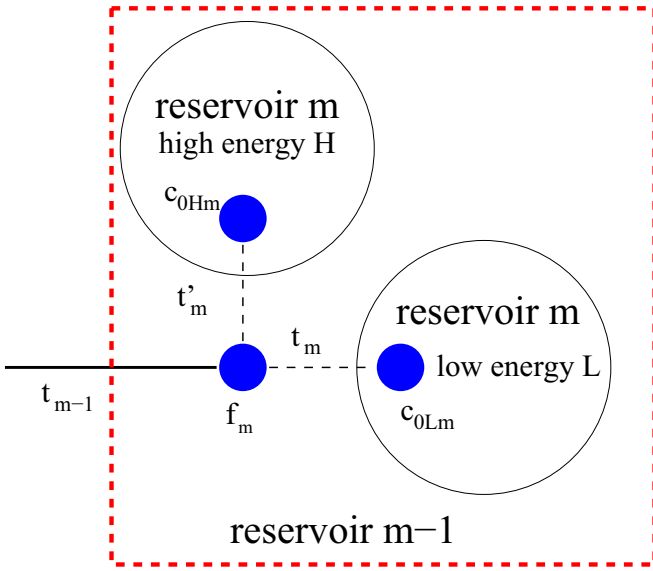

FIG. 3. In the modified recursion for the Wilson chain, we divided the reservoir m analog to Fig. 2(b) into its high-energy and low-energy (H and L, respectively) contributions, which are tailored such that the low-energy part is coupled to f_m with the matrix element $t_m < V_m$.

so $\Gamma_m(\omega) = \Gamma_m^L(\omega) + \Gamma_m^H(\omega)$. This step is schematically shown in Fig. 3. The cutoff energy scale $d_m \propto \lambda^{-m/2}$ must be self-consistently determined by the equation

$$t_m^2 = \frac{1}{\pi}\int_{-\infty}^{\infty} d\omega\, \Gamma_m^L(\omega - i\delta). \tag{25}$$

The precise value of d_m will depend on the analytical form of the specific cutoff function $F_d(\omega)$. The separate Hilbert transformation of $\Gamma_m^L(\omega)$ and $\Gamma_m^H(\omega)$ yields the corresponding real parts to $\Gamma_m^L(\omega) = \mathrm{Im}\Delta_m^L(\omega - i0^+)$ and $\Gamma_m^H(\omega) = \mathrm{Im}\Delta_m^H(\omega - i0^+)$.

Partitioning the new reservoir m into a high- and low-energy part,

$$H_{\mathrm{res}}(m) = H_{\mathrm{res}}^L(m) + H_{\mathrm{res}}^H(m), \tag{26}$$

the hybridization to the new chain site m also splits into two parts

$$H_I(m) = H_I^L(m) + H_I^H(m), \tag{27}$$

each involving only low- and, respectively, high-energy modes:

$$H_I^L(m) = t_m(f_m^\dagger c_{0Lm} + c_{0Lm}^\dagger f_m), \tag{28}$$

$$H_I^H(m) = t'_m(f_m^\dagger c_{0Hm} + c_{0Hm}^\dagger f_m). \tag{29}$$

The high-energy coupling constant t'_m accounts for the difference between V_m^2 and t_m^2: $t'_m = \sqrt{V_m^2 - t_m^2}$. The bath operators c_{0Lm} and c_{0Hm} are a linear combination of these new bath modes,

$$c_{0Lm} = \sum_k \lambda_{kLm} c_{kLm}, \quad c_{0Hm} = \sum_k \lambda_{kHm} c_{kHm}, \tag{30}$$

and also fulfill fermionic commutation relations. Their corresponding GFs are related to the coupling functions:

$$G_{c_{0Lm};c_{0Lm}^\dagger}(z) = \frac{1}{t_m^2}\Delta_m^L(z), \quad G_{c_{0Hm};c_{0Hm}^\dagger}(z) = \frac{1}{(t'_m)^2}\Delta_m^H(z). \tag{31}$$

After splitting the coupling function $\Delta_m(z)$ into a low- and high-energy part, we use $\tilde{\Delta}_m(z) = \Delta_m^L(z)$ in the next iteration step $m \to m+1$ via Eq. (20). Therefore, we have identified the coupling function $\tilde{\Delta}_{m-1}(z)$ introduced in Eq. (19) as the low-energy coupling function of the previous iteration, $\tilde{\Delta}_{m-1}(z) = \Delta_{m-1}^L(z)$.

It should be noted here that V_m is always larger than the desired Wilson chain coupling t_m for any $\Lambda > 1$ which ensures that the required reservoirs can be generated for any Wilson chain regardless of the choice of Λ. $V_0 > t_0 \forall \Lambda > 1$ can be shown analytically (see Appendix A). If our algorithm generated a $V_m^2 < t_m^2$, we would replace $t_m \to V_m$ implying that the chain site m does not couple to an auxiliary high energy reservoir, i.e., $t'_m = 0$.

By splitting each coupling function into high- and low-energy modes, the continuous fraction expansion has been modified such that by coupling a set of additional high-energy reservoirs $H_{\mathrm{res}}^H(m)$ to the chain site m of a Wilson chain, the original continuous coupling function is restored. The hybrid bath Hamiltonian

$$\tilde{H}_{\mathrm{bath}}(N) = H_{\mathrm{chain}}(N) + H_{\mathrm{res}}(N) + H_I(N) \tag{32}$$

with the additional reservoirs augmenting the Wilson chain $H_{\mathrm{chain}}(N)$,

$$H_{\mathrm{res}}(N) = \sum_{m=0}^{N-1}\sum_{\nu=1}^{M} H_{\mathrm{res},\nu}^H(m) + \sum_{\nu=1}^{M} H_{\mathrm{res},\nu}(N), \tag{33}$$

replaces the original H_{bath} without changing the impurity dynamics. This also defines the coupling $H_I(N)$ between the finite-size Wilson chain of length N and the reservoirs

$$H_I(N) = \sum_{m=0}^{N-1}\sum_{\nu=1}^{M} H_{I,\nu}^H(m) + \sum_{\nu=1}^{M} H_{I,\nu}(N). \tag{34}$$

Note that we have finally restored the flavor index ν, and the last chain site is coupled to the full unsplit reservoirs. The topology of this resulting hybrid Hamiltonian is depicted in Fig. 4. In the limit $\Lambda \to 1^+$, $t_{m\nu}^2$ approaches $V_{m\nu}^2$. As a consequence $t'_{m\nu} \to 0$, and the high energy reservoirs $H_{I,\nu}^H(m)$ decouple from the system. In this case, the hybrid Hamiltonian Eq. (32) approaches the DMRG tight-binding chain [74] augmented by a single reservoir at the end of the finite-size chain.

The hybrid bath Hamiltonian $\tilde{H}_{\mathrm{bath}}(N)$ consists of the following terms: the Wilson chain Hamiltonian $H_{\mathrm{chain}}(N)$ generated by the NRG [58], the individual high-energy reservoirs $H_{\mathrm{res},\nu}^H(m)$ at the energy scale d_m and $m < N$, the full remaining reservoir $H_{\mathrm{res},\nu}(N)$ for each flavor ν and, most importantly, the coupling between each Wilson chain site m and the corresponding reservoirs $H_I(N)$.

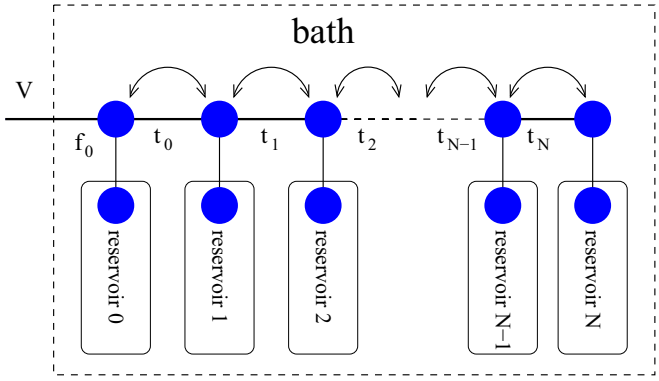

FIG. 4. The original bath is replaced by a Wilson chain where each chain site $m < N$ is coupled to a high-energy reservoir $H^H_{\rm res}(m)$ and the last site is connected to the remaining reservoir $H_{\rm res}(N)$.

D. Reservoir coupling functions $\Gamma_{\nu,m}(\omega)$

In principle, the recursion outlined in the previous section can be applied to any coupling function $\Gamma_\nu(\omega)$. In this paper, however, we restrict ourselves to the simplest case as a starting point of the recursion. Considering a constant density of states within the band $\omega \in [-D, D]$, the hybridization function takes the form

$$\Gamma(\omega) = \Gamma_0 \Theta(D - |\omega|), \tag{35}$$

with the charge fluctuation scale $\Gamma_0 = \frac{\pi V^2}{2D}$. The real part of $\Delta(z)$ is obtained via a Kramers-Kronig relation. Note that we dropped the bath flavor index ν since we focus on spin degenerate coupling functions in this paper.

If at each iteration the reservoir $\Delta(\omega)$ is split into a high-energy part $\Delta_H(\omega)$ and a low-energy part $\Delta_L(\omega)$ in such a way that the adequate Wilson chain coupling parameters t_m are generated, then the reservoir coupling functions become invariant at later iterations m if the frequency as well as the magnitude are rescaled by a factor of $\sqrt{\Lambda}$. The results for these rescaled coupling functions are depicted in Fig. 5. The two panels on the left hand side show the hybridization functions for the even iterations and the two panels on the right hand side for the odd iterations, respectively. Clearly, the recursion rapidly approaches convergence.

In deriving the leading order correction to the nonequilibrium dynamics in the presence of these additional reservoirs, the relaxation matrix acquires contributions of the type $\Gamma_m(E^{m_1}_{l_1} - E^{m_2}_{l_2})$, where the coupling function of the reservoir m must be evaluated at the energy difference between two NRG eigenenergies of two different energy shells m_1 and m_2. Taking into account the NRG energy hierarchy, we can conclude from Fig. 5 that $\Gamma_m(E^{m_1}_{l_1} - E^{m_2}_{l_2}) \approx 0$, if either $m_1 < m$ or $m_2 < m$.

III. NONEQUILIBRIUM DYNAMICS

The main focus of this paper is to derive a hybrid approach to the nonequilibirum dynamics of QISs. It combines the time-dependent renormalization group (TD-NRG) [50,51] with a Bloch-Redfield approach [24] which incorporates the effect of the couplings to the additional reservoirs neglected in the NRG onto the real-time dynamics.

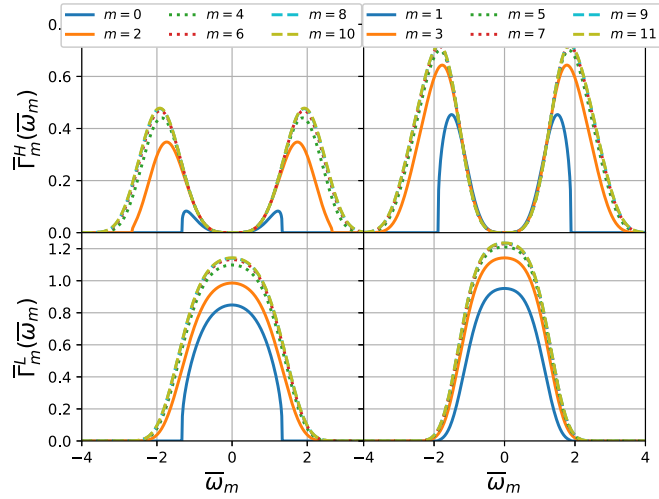

FIG. 5. Spectral functions $\bar{\Gamma}^{H/L}_m(\omega) = \mathrm{Im}\Delta^H_m(\omega - i0^+)/\omega_m$ of the high (at the top) and low (at the bottom) energy reservoirs vs $\bar{\omega}_m = \omega/\omega_m$. A bandwidth of $D = 100\,\Gamma_0$ and a discretization parameter $\Lambda = 2$ have been chosen. The sites of the chain that the particular reservoir is coupled to are counted by m.

A. Nonequilibrium dynamics in the discretized model: The TD-NRG

To set the stage, we review the TD-NRG which is the starting point of the hybrid approach to nonequilibrium. The TD-NRG was derived [50,51] as an extension of the NRG to access the nonequililibrium dynamics of QISs. The TD-NRG is designed to calculate the full nonequilibrium dynamics of a QIS after a sudden quench: $H(t) = H_0\Theta(-t) + H_f\Theta(t)$, but it is restricted to the discretized representation of the QIS. Recently, it was extended to a series of quenches [53] mimicking the discretization of time for a time-dependent Hamiltonian $H(t)$.

The initial state of the system is assumed to be in thermal equilibrium:

$$\rho_0 = \frac{e^{-\beta H_0}}{\mathrm{Tr}[e^{-\beta H_0}]}. \tag{36}$$

At time $t = 0$, the Hamiltonian suddenly switches and the time evolution is governed by the Hamiltonian H_f. We assume that the switching time is short compared to all relevant timescales in the QIS such that it can be viewed as instantaneous. Then, the time evolution of the density operator is given by

$$\rho(t > 0) = e^{-itH_f}\rho_0 e^{itH_f} \tag{37}$$

for a time-independent H_f. Using the complete basis set of the final Hamiltonian the time evolution of any local operator O is given by [50,51]

$$\langle O(t)\rangle = \sum_{m=m_{\rm min}}^{N} \sum_{r,s}^{\rm trun} e^{it(E^m_r - E^m_s)} O^m_{r,s} \rho^{\rm red}_{s,r}(m), \tag{38}$$

where E^m_r and E^m_s are the NRG eigenenergies of the Hamiltonian H_f at iteration $m \leqslant N$. $O^m_{r,s}$ is the matrix representation of the operator O at that iteration m [58]. $m_{\rm min}$ is the first iteration at which the many-body Hilbert space is truncated by the NRG approach. $\rho^{\rm red}_{s,r}(m)$ denotes the reduced density

matrix,

$$\rho^{\mathrm{red}}_{s,r}(m) = \sum_{e} \langle s, e; m|\rho_0|r, e; m\rangle, \tag{39}$$

in the basis of the final Hamiltonian where the chain DOF e of the chain sites $m' > m$ (which are called the environment here) are traced out. In Eq. (38), the restricted sums over r and s require that at least one of these states is discarded at iteration m: only the discarded states contribute to the dynamics at iteration m. The kept states $|k, e; m\rangle$ are refined by adding the chain link couplings to larger chain sites: The discarded states at a later iteration are formed from a linear combination of this tensor product basis. The temperature $T_N \propto \Lambda^{-N/2}$ of the TD-NRG calculation is defined by the length of the NRG Wilson chain N and enters Eq. (36).

The TD-NRG comprises two simultaneous NRG runs: one for the initial Hamiltonian H_0 to compute the initial density operator ρ_0 of the system in Eq. (36) and one for H_f to obtain the approximate eigenbasis governing the time evolution in Eq. (38).

This approach has also been extended to multiple quenches [53], time evolution of spectral functions [54], and steady state currents at finite bias [52,75,76]. The only error of this method originates from the representation of the bath continuum by a finite-size Wilson chain [64] and are essentially well understood [59,60].

Up to this point, the type of quench is not specified: The switching of $H(t)$ from H_0 to H_f could be a local quench or of global nature. Global quenches in infinitely large systems are conceptually complicated since they would imply an instantaneous change of a system with an infinite amount of energy. In experiments, such changes can only occur on a finite timescale and they spread at a speed whose upper bound is the speed of light.

Throughout this paper, we focus on local quenches where all fermionic baths share the same chemical potential. Note, however, that a local quench does not necessarily imply a relaxation to a thermal equilibrium in the long-time limit. The most prominent example is a quantum dot coupled to two leads at different chemical potentials. Such a system relaxes into a nonequilibrium current carrying steady state after switching on the tunneling matrix elements between the leads and the quantum dot [77,78]. Such situations are accessible to our approach presented in the next section but are not investigated in this paper.

B. Bloch-Redfield extension of the TD-NRG

1. Introduction

Finite-size oscillations remain present in the TD-NRG expectation value $\langle O\rangle(t)$ calculated via Eq. (38) even for $t \to \infty$ depending on the NRG discretization parameters [59,60,79]. This is a generic feature of accurately calculating the quantum dynamics in finite-size systems, here on a Wilson chain of length $N+1$. We define the averaged steady-state value,

$$\begin{aligned}\langle O\rangle_\infty &= \lim_{T\to\infty} \frac{1}{T}\int_0^T dt\, \langle O\rangle(t) \\ &= \sum_{m=m_{\min}}^{N} \sum_{r,s}^{\mathrm{trun}} O^m_{r,s}\rho^{\mathrm{red}}_{s,r}(m)\delta_{E_s,E_r},\end{aligned} \tag{40}$$

predicted by the TD-NRG, implying that r and s have to be discarded states. This eliminates the finite-size oscillations present in $\langle O\rangle(t)$ in the long-time limit. Only the energy diagonal matrix elements contribute to the steady state, which has been extensively discussed in the context of the eigenstate thermalization hypothesis [80–83].

Since the contribution of the discarded states of the iterations $m < N$ to the thermodynamic density operator in the NRG is negligibly small, a thermalized averaged steady state implies vanishing contributions from all $\rho^{\mathrm{red}}_{s,r}(m)$ with $m < N$ and an approach of $\rho^{\mathrm{red}}_{s,r}(N) \to \delta_{E^N_s,E^N_r}\exp(-\beta E^N_s)/Z$. Within the TD-NRG, the values of the matrix elements $\rho^{\mathrm{red}}_{s,r}(m)$, however, remain fixed and depend on the initial condition [80–83]. The difference $\Delta O = \langle O\rangle_\infty - \langle O\rangle_{th}$ quantifies the deviation of the TD-NRG steady-state prediction from the thermodynamic limit $\langle O\rangle_{\mathrm{th}}$.

In Sec. II C, we have proven that the Hamiltonian $\tilde{H}_{\mathrm{bath}}(N)$, comprising the Wilson chain with N chain links and a sequence of reservoirs, generates the same coupling function $\Gamma_\nu(\omega)$ as the original continuum problem. Hence, the Hamiltonian $H'(N)$,

$$H'(N) = H^{\mathrm{NRG}}_N + H_{\mathrm{res}}(N) + H_I(N), \tag{41}$$

is equivalent to the original Hamiltonian H,

$$H = H_{\mathrm{imp}} + H_I + H_{\mathrm{bath}}, \tag{42}$$

prior to the Wilson discretization with respect to its impurity dynamics. $H'(N)$ augments the standard NRG Hamiltonian of a chain of length N, H^{NRG}_N, with the sum of all additional reservoirs $H_{\mathrm{res}}(N)$ and their couplings to the chain links $H_I(N)$ as stated in detail in Eq. (34).

The TD-NRG [50,51] utilizes the standard NRG approximation by replacing the original Hamiltonian with the approximation $H \to H^{\mathrm{NRG}}_N$. The aim of this Sec. III B is to derive a set of coupled differential equations for the dynamics of the reduced density matrix $\rho^{\mathrm{red}}_{s,r}(m)$ in Eq. (38): $\rho^{\mathrm{red}}_{s,r}(m) \to \rho^{\mathrm{red}}_{s,r}(m,t)$. The physical origin of the time dependency of the reduced density matrix is the coupling of the Wilson chain to a set of reservoirs neglected in the NRG approximation. While the exact solution of $\rho^{\mathrm{red}}_{s,r}(m,t)$ in the presence of the additional reservoirs is complicated and impractical to implement, we gear toward an approximate solution in the spirit of weak coupling theories such as a Bloch-Redfield or Lindblad type of master equations [24,40].

One can explicitly show [24,40] that the dynamics of the diagonal elements of the density matrix defined on a finite Hilbert space of dimension D decouples from the off-diagonal dynamics within the Bloch-Redfield or Lindblad approaches. The Liovillian operator has D^2 eigenvalues: D of them determine the decay into the steady state while the other $D^2 - D$ eigenvalues are complex and always come in pairs λ_i, λ_i^*, since the density matrix must be Hermitian.

Below we derive these two types of differential equations for the diagonal and the off-diagonal matrix elements of $\rho^{\mathrm{red}}_{s,r}(m,t)$. We show that for a generic decay tensor, the diagonal matrix elements approach the thermal equilibrium defined by the full density matrix formulation [84] of the NRG while the off-diagonal matrix elements vanish in the long-time limit. To ensure the conservation of the trace of

the density operator, the differential equation for the diagonal matrix elements requires a coupling of all energy shells, i.e., all iterations m. This sets a practical limit to our approach and additional approximations are required since the implementation of the couplings between all energy shells is practically impossible.

2. Derivation of the second-order corrections to the TD-NRG dynamics

We initially start from the total density operator in the interaction representation,

$$\rho_I(t) = e^{iH_0 t}\rho(t)e^{-iH_0 t}, \tag{43}$$

where $H_0 = H_N^{\rm NRG} + H_{\rm res}(N)$. The total density operator encodes the dynamics of the original problem and operates on the Wilson chain DOF as well as the DOF of the reservoirs. Neglecting the system-reservoir coupling $H_I(N)$ and assuming a factorized density operator in the contributions of each subsystem yields a time-independent density operator whose reduced matrix elements relevant for the local expectation values are given by the TD-NRG values $\rho_{s,r}^{\rm red}(m)$. By incorporating the additional system-reservoir coupling, the density operator $\rho_I(t)$ acquires the time dependency that we cast into a master equation for $\rho_{s,r}^{\rm red}(m,t)$.

The dynamics of the density operator $\rho_I(t)$ is governed by the differential equation

$$\partial_t \rho_I(t) = i[\rho_I(t), V_I(t)] \tag{44}$$

in the interaction picture, where the system-reservoir coupling takes the form

$$V_I(t) = e^{iH_0 t}H_I(N)e^{-iH_0 t}. \tag{45}$$

For expectation values of local operators, it is sufficient to know $\rho_S(t) = {\rm Tr}_R[\rho_I(t)]$, where we have traced out all the reservoir degrees of freedom. This operator is acting only on the Wilson chain or system S.

Now we can adapt Eq. (44) to derive a Bloch-Redfield equation for the reduced density matrix $\rho_S(t)$. The individual steps are carried out in Appendix B and can also be found in textbooks—for example, Ref. [24].

The derivation requires a complete eigenbasis [24] of the discrete system Hamiltonian H_S which is equal to $H_{\rm NRG}(N)$. For a given NRG eigenbasis $|r,e;m\rangle$ of the discrete Hamiltonian $H_S = H_N^{\rm NRG}$, the Bloch-Redfield master equation reads

$$\dot\rho_{1,2}(t) = -\sum_{3,4} R_{1,2;3,4}(t)\rho_{3,4}(t), \tag{46a}$$

$$R_{1,2;3,4}(t) = \delta_{2,4}\sum_5 \Xi^+_{1,5,5,3}(t) + \delta_{1,3}\sum_5 \Xi^-_{4,5,5,2}(t) - \Xi^+_{4,2,1,3}(t) - \Xi^-_{4,2,1,3}(t), \tag{46b}$$

$$\Xi^+_{1,2,3,4}(t) = e^{i(\omega_{1,2}+\omega_{3,4})t}\sum_{\tilde m=0}^{N}\sum_\nu [C_{\nu,\tilde m}(\omega_{3,4})(f^\dagger_{\nu,\tilde m})_{1,2}(f_{\nu,\tilde m})_{3,4} + \bar C_{\nu,\tilde m}(\omega_{3,4})(f_{\nu,\tilde m})_{1,2}(f^\dagger_{\nu,\tilde m})_{3,4}], \tag{46c}$$

$$\Xi^-_{1,2,3,4}(t) = e^{i(\omega_{1,2}+\omega_{3,4})t}\sum_{\tilde m=0}^{N}\sum_\nu [C^*_{\nu,\tilde m}(\omega_{2,1})(f^\dagger_{\nu,\tilde m})_{1,2}(f_{\nu,\tilde m})_{3,4} + \bar C^*_{\nu,\tilde m}(\omega_{2,1})(f_{\nu,\tilde m})_{1,2}(f^\dagger_{\nu,\tilde m})_{3,4}], \tag{46d}$$

with the energy differences $\omega_{i,j} = E_i - E_j$. The index $i \in \{1,2,3,4,5\}$ is a general shortcut notation for the tuple $i = (r_i, e_i, m_i)$, where r_i is a state label of the NRG state at iteration m_i, and e_i is an environment degree of freedom of the remaining $N - m_i$ chain sites. $e^{i\omega_{i,j}t}(f^{(\dagger)}_{\nu,\tilde m})_{i,j} = \langle r_i, e_i; m_i|\, f^{(\dagger)}_{\nu,\tilde m}(t)\,|r_i, e_i; m_i\rangle$ denotes the factorisation of the time-dependent matrix element of the $\tilde m$th chain site into a time-independent part and a time-dependent phase factor. The index $\tilde m$ labels the reservoir index of the sum over all additional reservoirs in $H_I(N)$.

The bath coupling functions $\Gamma_{\nu m}(\epsilon)$ derived in Sec. II C enter the expression as the greater and the lesser GF for each reservoir $G^>_{\nu,m}(\tau)/G^<_{\nu,m}(\tau)$ and fully determine the effects of the reservoirs onto the dynamics of the Wilson chain. The correlation functions $C_{\nu,m}(\omega)$ and $\bar C_{\nu,m}(\omega)$ are obtained by a half-sided Fourier transformation,

$$C_{\nu,m}(\omega) = i\int_0^\infty d\tau G^>_{\nu,m}(\tau)e^{-i\omega\tau}, \tag{47a}$$

$$\bar C_{\nu,m}(\omega) = -i\int_0^\infty d\tau G^<_{\nu,m}(\tau)e^{-i\omega\tau}, \tag{47b}$$

that results from integrating Eq. (44) and then substituting the resulting expression for $\rho_I(t)$ back into Eq. (44). Using the definitions of the lesser and the greater GFs introduced in Eqs. (B7), we find

$$C_{\nu,m}(\omega) + C^*_{\nu,m}(\omega) = iG^>_{\nu,\tilde m}(-\omega), \tag{48a}$$

$$\bar C_{\nu,m}(\omega) + \bar C^*_{\nu,m}(\omega) = -iG^>_{\nu,\tilde m}(\omega), \tag{48b}$$

which relates these combinations to the Fourier transformation of the equilibrium greater and lesser reservoir coupling functions.

3. Secular approximation

The objective is to derive a differential equation for the reduced density matrix $\rho_{s,r}^{\rm red}(m;t)$ using Eqs. (46) and to replace $\rho_{s,r}^{\rm red}(m)$ by its solution $\rho_{s,r}^{\rm red}(m;t)$. The Bloch-Redfield equations introduced in the previous section serve as a starting point for a master equation describing the dynamics of the reduced density matrix $\rho_{s,r}^{\rm red}(m;t)$, which is defined as

$$\rho_{s,r}^{\rm red}(m;t) = \sum_e \langle s,e;m|\rho_S(t)|r,e;m\rangle, \tag{49}$$

with $\rho^{\rm red}_{s,r}(m) = \rho^{\rm red}_{s,r}(m;t=0)$ as the initial condition. The index pair (s,r) can either label both discarded states or contain only one discarded state, so we have to allow for the second state to be retained for the next NRG iteration. Both, however, are approximate eigenstates of H_S, $H_S|r,e;m\rangle \approx E^m_r|r,e;m\rangle$ and $H_S|s,e;m\rangle \approx E^m_s|s,e;m\rangle$.

In the next step, we apply the secular approximation [24,40]. The remaining explicit time dependency on the r.h.s of Eq. (46a) in terms of fast oscillating phases, which only occurs in Eqs. (46c) and (46d), must vanish, providing the additional energy constraint

$$e^{i(\omega_{1,2}+\omega_{3,4})t} \to \delta_{\omega_{1,2},-\omega_{3,4}}, \tag{50}$$

which is consistent with a slowly varying reduced density matrix. As a consequence, the time-dependent tensor $R_{1,2,3,4}(t)$ becomes time independent.

For the dynamics of $\rho^{\rm red}_{s,r}(m;t)$, only the case $m_1 = m_2$ is relevant. The resulting condition $E^{m_1}_{r_1} - E^{m_1}_{r_2} = E^{m_3}_{r_3} - E^{m_4}_{r_4}$ requires the discussion of two cases (given that degeneracies in r_1, r_2 are excluded): For the diagonal elements, $r_1 = r_2$, immediately $m_3 = m_4$ and $r_3 = r_4$ follow (since it is highly unlikely to find two different eigenstates at different iterations $m_3 \neq m_4$ that are energetically degenerate.)

If $r_1 \neq r_2$, and thus $E^{m_1}_{r_1} - E^{m_1}_{r_2} \neq 0$, the equation can only be fulfilled for $m_1 = m_2 = m_3 = m_4$, since it is very unlikely to find the same energy difference on two different NRG iterations.

From this discussion, we draw two important conclusions: (i) For the occupation dynamics given by the diagonal elements of the density matrix $\rho^{\rm red}_I(t)$ (DDM), we obtain Bloch-Redfield tensor matrix elements $R_{1,2,3,4}$ that couple two different iterations $m = m_1 = m_2$ and $m' = m_3 = m_4$. (ii) The dynamics of the off-diagonal elements of the density matrix (ODDM) is determined by the coupling to the reduced density operator within the same energy shell m.

C. Dynamics of the reduced density matrix $\rho^{\rm red}_{s,r}(m)$

Within the Bloch-Redfield approach [24], the DDM decouple from the ODDM. The DDM describe the occupation dynamics and are coupled by relaxation parameters within the same iteration index m as well as by terms connecting different iterations. These later terms are important for deriving a master equation for the occupation dynamics that satisfies the conservation of the trace of the density matrix at all times.

Guided by the energy separation between the discarded states and the kept states which provide the span of the Fockspace for all discarded states at later iterations, we use the approximation

$$\langle r,e;m|\,\rho_S(t)\,|s,e';m\rangle \approx \rho^{\rm red}_{r,s}(m;t)\delta_{e,e'}d^{-(N-m)} \tag{51}$$

for the matrix elements of the reduced density operator $\rho_S(t)$ which strictly holds only for the equilibrium density operator [84]. Once we trace out the environment DOF e, the factor $d^{-(N-m)}$ is canceled and the definition of $\rho^{\rm red}_{r,s}(m;t)$ introduced in Eq. (49) is recovered.

1. Diagonal part of the reduced density matrix

To evaluate the DDM, $1 = 2$, $3 = 4$ has to be set in Eq. (46) to arrive at

$$\dot\rho^{\rm red}_{l_1,l_1}(m_1;t) = \sum_{l_2,m_2}\big(\Xi_{l_2,l_1}(m_2,m_1)\rho^{\rm red}_{l_2,l_2}(m_2;t) - \Xi_{l_1,l_2}(m_1,m_2)\rho^{\rm red}_{l_1,l_1}(m_1;t)\big), \tag{52}$$

with the relaxation matrix elements

$$\Xi_{l_1,l_2}(m_1,m_2) = d^{-(N-m_1)}\sum_{e_1,e_2}(\Xi^+_{1,2,2,1} + \Xi^-_{1,2,2,1}).$$

Equation (51) demands that $e_1 = e_2$ as well as $e_3 = e_4$ in Eq. (46). Thus, only terms of the form $\langle r,e;m|\,\rho_S(t)\,|s,e;m\rangle$ occur in Eq. (46), and the environment e_1 has been traced out on both sides of Eq. (52). Note that the DDM are restricted to the discarded states l_i of the iteration m_i, since the complete basis set used to evaluate the trace of the density matix comprises all discarded states [50,51] and a combination of two kept states does not contribute in Eq. (38).

For the DDM, the relations between the different half-sided Fourier components in systems with identical chemical potentials in each reservoir

$$C_{\nu,\tilde m}(\omega_{2,1}) + C^*_{\nu,\tilde m}(\omega_{2,1}) = 2f(\omega_{2,1})\Gamma_{\nu,\tilde m}(\omega_{1,2}),$$
$$\overline{C}_{\nu,\tilde m}(\omega_{2,1}) + \overline{C}^*_{\nu,\tilde m}(\omega_{2,1}) = 2f(\omega_{2,1})\Gamma_{\nu,\tilde m}(\omega_{2,1}),$$

are used—see also Eq. (48)—to derive the explicit expression of the relaxation tensor matrix elements

$$\Xi_{l_1,l_2}(m_1,m_2) = \frac{2f(\omega_{2,1})}{d^{N-m_1}}\big(W^{(m_1,m_2)}_{l_1,l_2} + W^{(m_2,m_1)}_{l_2,l_1}\big), \tag{53}$$

$$W^{(m_1,m_2)}_{l_1,l_2} = \sum_{\tilde m=0}^{M}\sum_{\nu}\Gamma_{\nu,\tilde m}(\omega_{1,2})X^{\tilde m}_{l_1,l_2}(m_1,m_2), \tag{54}$$

$$X^{\tilde m}_{l_1,l_2}(m_1,m_2) = \sum_{e_1,e_2}\langle l_1,e_1;m_1|f^\dagger_{\nu,\tilde m}|l_2,e_2;m_2\rangle \times \langle l_2,e_2;m_2|f_{\nu,\tilde m}|l_1,e_1;m_1\rangle, \tag{55}$$

where in general the number of reservoirs is determined by the chain length, i.e., $M = N$. The first term on the r.h.s of Eq, (53) describes the emission of a particle into the reservoir $\tilde m$ and afterward a reabsorption while the second term starts with an absorption and ends with a reemission process.

It is easy to check that the sum $W^{(m_1,m_2)}_{l_1,l_2} + W^{(m_2,m_1)}_{l_2,l_1}$ is symmetric with respect to exchanging the label pairs $(l_1,m_1) \leftrightarrow (l_2,m_2)$. Therefore, the asymmetry in the rates $\Xi_{l_1,l_2}(m_1,m_2)$ with respect to this index swap is solely caused by the prefactor.

The steady-state value of the reduced density matrix is fully determined by the prefactor $f(\omega_{2,1})d^{m_1-N}$. The specific form of the remaining term $W^{(m_1,m_2)}_{l_1,l_2} + W^{(m_2,m_1)}_{l_2,l_1}$ is irrelevant for the steady-state values and only influences the relaxation timescales as long as all matrix elements remain coupled in this master equation. Therefore, a decoupling of bound states on the Wilson chain from the reservoir continuum would lead to a steady state of the system which deviates from the thermal equilibrium.

We discuss two important properties of the master equation, Eq. (52). First, the trace $\mathrm{Tr}[\rho_S] = \sum_{l,m}\rho^{\rm red}_{l,l}(m;t)$ is

conserved at all times t, since

$$0 = \partial_t \mathrm{Tr}[\rho_S] = \sum_{l_1,m_1} \dot{\rho}^{\mathrm{red}}_{l_1,l_1}(m_1;t)$$
$$= \sum_{l_1,m_1}\sum_{l_2,m_2} \big(\Xi_{l_2,l_1}(m_2,m_1)\rho^{\mathrm{red}}_{l_2,l_2}(m_2;t)$$
$$- \Xi_{l_1,l_2}(m_1,m_2)\rho^{\mathrm{red}}_{l_1,l_1}(m_1;t)\big). \tag{56}$$

This can be seen by interchanging the summation indices (l_1, m_1) and (l_2, m_2) in the second summation.

Second, the steady state of the matrix elements obeys the detailed balance condition. Since $f(\omega_{2,1})e^{-\beta E_{l_1}} = f(\omega_{1,2})e^{-\beta E_{l_2}}$ holds, and thus $\Xi_{l_1,l_2}(m_1,m_2)e^{-\beta E_{l_1}} = \Xi_{l_2,l_1}(m_2,m_1)e^{-\beta E_{l_2}}d^{m_1-m_2}$, the fixed point of Eq. (52) is given by

$$\rho^{\mathrm{red}}_{l,l}(t\to\infty;m) = \frac{d^{N-m}}{Z}e^{-\beta E^m_l}, \tag{57}$$

with the partition sum Z [84]:

$$Z = \sum_{m=m_{\min}}^{N}\sum_{l} d^{N-m}e^{-\beta E^m_l}. \tag{58}$$

The formalism requires that E^m_l is given in the absolute energy units measured relative to the ground-state energy on the last iteration E^N_g, which comprises the sum of the rescaled NRG eigenenergies $\bar{E}^m_l$ and the ground-state energy shift relative to the last iteration, $\Delta E^{N,m}_g = E^m_g - E^N_g$. Since the ground-state energy is reduced in each iteration step, a positive constant is added to $E^m_l = \Lambda^{(m-1)/2}\bar{E}^m_l$, which in combination with the low temperature $1/\beta$ causes an exponential suppression of the contributions for $m < N$ even for $\bar{E}^m_l = 0$ on the specific iteration m after identifying $\beta = \beta_N \propto \Lambda^{(N-1)/2}\bar{\beta}$ [58].

The steady-state fixed point stated in Eq. (57) is independent of the values of $X_{l_1,l_2}(m_1,m_2)$ unless some matrix elements vanish. Therefore, $\rho^{\mathrm{red}}_{l,l}(m;t)$ in general approaches its thermal equilibrium value. If, however, the reservoirs have different chemical potentials, this statement does not hold. In that case, the structure of the master equation suggests the approach to a steady state that differs from thermal equilibrium [41,42].

The calculation of all matrix elements of the fourth-order tensor $\Xi_{l_1,l_2}(m_1,m_2)$ for all combinations of discarded states between all iterations m_1, m_2 is numerically very expensive since for every Wilson chain site $\tilde{m}$ one needs to build $X^{\tilde{m}}_{l_1,l_2}(m_1,m_2)$ [see Eq. (55)] for each $m_1, m_2 \in [m_{\min}, N]$, which scales as $N_S^5N^3$ as outlined in the next section. Thus, this procedure appears to not be feasible. Therefore, we hereinafter propose further approximations that do not violate the conservation of the trace as well as the thermalization of the density matrix but keep the approach manageable even for large Fock spaces.

First, we restrict the summation of the reservoirs in Eqs. (46c) and (46d) and, in particular, in Eq. (53) to $\tilde{m} \leqslant M = \min(m_1, m_2)$. This is a consequence of the analytic properties of the coupling functions $\Gamma_{\nu,\tilde{m}}(\omega)$ discussed at the end of Sec. II D.

2. Calculation of the matrix elements $\Xi_{l_1,l_2}(m_1,m_2)$

The key ingredient of the master equation is the calculation of the transition rates $\Xi_{l_1,l_2}(m_1,m_2)$ as defined in Eq. (53). While it is straightforward to evaluate the expressions for $m_1 = m_2$, it is a challenge to connect different Wilson shells. Therefore, we focus on $m_1 \neq m_2$ in the following.

We make use of the NRG hierarchy, implying that $f(E^{m_2}_{l_2} - E^{m_1}_{l_1}) \approx \Theta(m_2 - m_1)$. This implies that the density matrix element $\rho^{\mathrm{red}}_{l_1,l_1}(m_1;t)$ in Eq. (52) decays only into states with smaller energies, i.e., $m_2 \geqslant m_1$. The first term on the r.h.s of this equation is a source term which increases the occupation of the state l_1 via the decay of states l_2 from iterations $m_2 \leqslant m_1$.

Using the properties of the coupling functions $\Gamma_{\nu,\tilde{m}}(\omega)$ further justifies the simplification:

$$\Gamma_{\nu,\tilde{m}}(\pm\Delta E) \approx \begin{cases} \Gamma_{\nu,\tilde{m}}\big(\mp E^{m_1}_{l_1}\big) & \text{for } \tilde{m} \leqslant m_1 \\ 0 & \text{for } \tilde{m} > m_1. \end{cases} \tag{59}$$

To proceed, we use

$$1^-_m = \sum_{m'=m_{\min}}^{m}\sum_{l,e} |l,e;m'\rangle\,\langle l,e;m'| \tag{60}$$

and

$$1^+_m = \sum_{k,e} |k,e;m\rangle\langle k,e;m| \tag{61}$$

to partition the completeness relation [50,51]

$$1 = 1^-_m + 1^+_m\,, \tag{62}$$

of the Fock space of the Wilson chain. Since discarded states at a later iteration $m_2 > m_1$ only have an overlap with the kept states after the iteration m_1, we need to evaluate

$$X^{\tilde{m}}_{l_1,l_2}(m_1,m_2) = \sum_{e_1,e_2}\sum_{k,e}\sum_{k',e'} \langle l_1,e_1;m_1|\, f^\dagger_{\nu,\tilde{m}}|k,e;m_1\rangle$$
$$\times\langle k,e;m_1|l_2,e_2;m_2\rangle\,\langle l_2,e_2;m_2|\,k',e';m_1\rangle$$
$$\langle k',e';m_1|f_{\nu,\tilde{m}}|l_1,e_1;m_1\rangle, \tag{63}$$

from which $X^{\tilde{m}}_{l_2,l_1}(m_2,m_1)$ can be derived by exchanging the operators f and $f^\dagger$.

Then the matrix elements of the creation and annihilation operator are diagonal in the environment variables e_1, e, and e',

$$\langle l_1,e_1;m_1|\, f^\dagger_{\nu,\tilde{m}}|k,e;m_1\rangle = \delta_{e_1,e}(f^\dagger_{\nu,\tilde{m}})_{l_1,k}, \tag{64}$$

$$\langle k',e';m_1|f_{\nu,\tilde{m}}\,|l_1,e_1;m_1\rangle = \delta_{e_1,e'}(f_{\nu,\tilde{m}})_{k',l_1}, \tag{65}$$

leaving the calculation of the general overlap matrix elements

$$S^{(m_1,m_2)}_{l_2,l_2';k,k'} = \sum_{e_1,e_2}\langle k,e_1;m_1|l_2,e_2;m_2\rangle\,\langle l_2',e_2;m_2|\,k',e_1;m_1\rangle, \tag{66}$$

where we set $l_2 = l_2'$ at the end. This can most easily be evaluated in terms of a matrix product formulation [57].

We recall that the NRG eigenstates at the iteration $m_1 + 1$ can be expanded as

$$|r, e; m+1\rangle = \sum_{k,\alpha} P^m_{r,k}[\alpha]|k, \alpha, e; m\rangle, \tag{67}$$

where k denotes the kept states after the iteration m and α labels the DOF of the chain site $m+1$. The matrix $P^m_{r,k}[\alpha]$ is generated during the diagonalization of H^{NRG}_{m+1}. Recursively applying this relation leads to the matrix product expansion

$$|l_2, e_2; m_2\rangle = \sum_k \sum_{\{\alpha_i\}} \prod_{i=m_1}^{m_2-1} \mathbf{P}^{\mathbf{i}}[\alpha_i]|k, \{\alpha_i\}, e_2; m_1\rangle, \tag{68}$$

which we insert into Eq. (66) to obtain the overlap tensor:

$$S^{(m_1,m_2)}_{l_2,l_2';k,k'} = d^{N-m_2} \sum_{\{\alpha_i\}} \left[\prod_{i=m_1}^{m_2-1} \mathbf{P}^{\mathbf{i}}[\alpha_i]\right]_{l_2,k} \left[\prod_{i=m_1}^{m_2-1} \mathbf{P}^{\mathbf{i}}[\alpha_i]\right]^*_{l_2',k'}. \tag{69}$$

The prefactor d^{N-m_2} arises from performing the summation over the remaining diagonal environment DOF.

The calculation of $S^{(m_1,m_2)}_{l_2,l_2';k,k'}$ can be casted in the recursion relation

$$S^{(m_1,m_2+1)}_{l_2,l_2';k,k'} = \frac{1}{d} \sum_{\alpha_{m_2+1}} \sum_{k_1,k_2} P^{m_2+1}_{l_2,k_1}[\alpha_{m_2+1}]\left[P^{m_2+1}_{l_2',k_2}[\alpha_{m_2+1}]\right]^* S^{(m_1,m_2)}_{k_1,k_2;k,k'}. \tag{70}$$

Although this expression can be diagrammatically visualised in terms of matrix product states [57]. such a tensor with six indices is numerically not manageable and can only serve as an auxiliary quantity.

The recursion relation of the tensor $S^{(m_1,m_2+1)}_{l_2,l_2';k,k'}$, however, allows us to derive a recursion relation for the decay rates $W_{l_1,l_2}(m_1, m_2)$ defined in Eq. (54). For that purpose, we introduce the tensor

$$F_{k,k'}(l_1, m_1) = \sum_{\tilde{m}=0}^{m_1} \sum_{\nu} \Gamma_{\nu,\tilde{m}}\left(E^{m_1}_{l_1}\right)(f^\dagger_{\nu,\tilde{m}})_{l_1,k}(f_{\nu,\tilde{m}})_{k',l_1}. \tag{71}$$

This includes all reservoir coupling functions up to $\tilde{m} \leqslant m_1$. Due to the analytic properties of $\Gamma_{\nu,\tilde{m}}(\omega)$, we expect that $\Gamma_{\nu,\tilde{m}}(E^{m_1}_{l_1})$ is rapidly vanishing for $\tilde{m} \ll m_1$, so $\tilde{m} = m_1$ will be the major contribution. From the definition of $W_{l_1,l_2}(m_1, m_2)$, we immediately obtain

$$W_{l_1,l_2}(m_1, m_1) = d^{N-m_1} F_{l_2,l_2}(l_1, m_1) \tag{72}$$

for the Bloch-Redfield tensor elements connecting states on the same Wilson shell $m_1 = m_2$. The prefactor d^{N-m_1} arises from the trace over the remaining environment DOFs and compensates the prefactor $d^{-(N-m_1)}$ in $\Xi_{l_1,l_2}(m_1, m_2)$. Let us absorb the prefactor $d^{-(N-m_1)}$ in the definition

$$\frac{1}{d^{N-m_1}} W_{l_1,l_2}(m_1, m_2) = A^{(m_2,m_1)}_{l_2,l_2;l_1}, \tag{73}$$

where the tensor $A^{(m_2,m_1)}_{l_2,l_2;l_1}$ is given by the contraction of the overlap tensor $\mathbf{S}$ and the coupling tensor $\mathbf{F}(m_1)$:

$$A^{(m_2,m_1)}_{r,s;l_1} = \frac{1}{d^{N-m_1}} \sum_{k,k'} S^{(m_1,m_2)}_{r,s;k,k'} F_{k,k'}(l_1, m_1). \tag{74}$$

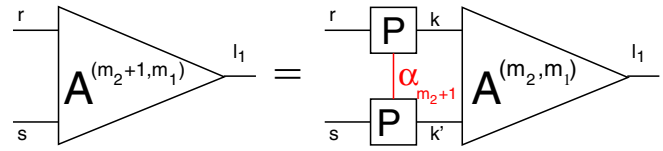

FIG. 6. Diagrammatic representation of the recursion relation for calculating the **A** tensor. Each box represents a matrix element $P_{r_{m_2+1},k_{m_2}}[\alpha_{m+1}]$ (upper row) or its complex conjugate (lower row). The state labels k and k' are plotted horizontally. The state label α_{m_2+1} for the $m+1$ site is plotted vertically. A connected line indicates a summation over the corresponding index in analogy to Fig. 2 in Ref. [51].

This **A** tensor obeys the recursion

$$A^{(m_2+1,m_1)}_{r,s;l_1} = \frac{1}{d} \sum_{\alpha_{m_2+1}} \sum_{k_1,k_2} P^{m_2+1}_{r,k_1}[\alpha_{m_2+1}]\left[P^{m_2+1}_{s,k_2}[\alpha_{m_2+1}]\right]^* A^{(m_2,m_1)}_{k_1,k_2;l_1}, \tag{75}$$

using the tensor $F_{k,k'}(l_1, m_1)$ as the initial condition, derived from the recursion Eq. (70). This recursion is visualized in Fig. 6.

Since the coupling tensor $\mathbf{F}(m_1)$ has been included in the definition, the A tensor has three indices for each combination (m_1, m_2) of iterations. Note that the prefactor in $S(m_1, m_2)$, d^{N-m_2}, can be combined with the overall prefactor of $\Xi_{l_1,l_2}(m_1, m_2)$, $d^{-(N-m_1)}$, to obtain $d^{-(m_2-m_1)}$ which only depends on the relative distance between the iterations. After calculating $A_{r,s;m_2}(l_1, m_1)$ for all states r, s present at iteration m_2, the diagonal matrix elements of discarded states, $A_{l_2,l_2;m_2}(l_1, m_1)$, enter the master equation while the kept sector, $A_{k,k';m_2}(l_1, m_1)$, is used in the recursion Eq. (75).

Inspecting of $X^{\tilde{m}}_{l_2,l_1}(m_2, m_1)$ in the definition Eq. (55) reveals that the only difference in the calculation is the combination of annihilation and creation operators. We include this difference into the tensor $\tilde{F}$,

$$\tilde{F}_{k,k'}(l_1, m_1) = \sum_{\tilde{m}=0}^{m_1} \sum_{\nu} \Gamma_{\nu,\tilde{m}}\left(-E^{m_1}_{l_1}\right)(f_{\nu,\tilde{m}})_{l_1,k}(f^\dagger_{\nu,\tilde{m}})_{k',l_1}, \tag{76}$$

which differs from Eq. (71) by the exchange of matrices for $f \leftrightarrow f^\dagger$ and the sign of the energy. By adding $\tilde{F}_{k,k'}(l_1, m_1)$ and $F_{k,k'}(l_1, m_1)$ and using this sum as initial condition in Eq. (75) generates recursively the sum $W^{(m_1,m_2)}_{l_1,l_2} + \tilde{W}^{(m_1,m_2)}_{l_1,l_2}$ after setting $r, s = l_2$.

This allows, in principle, to recursively evaluate $W_{l_1,l_2}(m_1, m_2)$ and, therefore, $\Xi_{l_1,l_2}(m_1, m_2)$. The calculation of all matrix elements $A^{(m_2+1,m_1)}_{r,s;l_1}$ for a fixed starting iteration m_1 in Eq. (75) requires typically N recursions for each m_1, and we need to calculate the matrix elements for N different m_2 as well as N different reservoirs $\tilde{m}$ so the calculation scales as $N^3 d N_S^5$. This is beyond a reasonable computational effort to calculate small corrections to the weakly time-dependent reduced density matrix elements.

3. Approximations of the rates for the diagonal master equation

Although the calculation of each matrix element for the diagonal parts of the Bloch-Redfield tensor is analytically straightforward and can be casted into the diagrammatical

matrix product state recursion depicted in Fig. 6, we want to point out that one needs a third-order tensor $A_{r,s;m_2}(l_1,m_1)$ at any time of the calculations. Although the recursions for calculating the sequence of tensors $A_{r,s;m_2}(l_1,m_1)$ for a fixed value m_1 can be independently evaluated for each start iteration m_1, running these calculations in parallel requires a large number of such tensors in the memory at any given time. Therefore, it might be more feasible to run the recursion for each m_1 sequentially and use highly parallelized matrix multiplication libraries.

However, in this paper, we have chosen a different approach. Consider that the correct Boltzmann distribution is enforced by the prefactor of $\Xi_{l_1,l_2}(m_1,m_2)$, $f(E^{m_2}_{l_2}-E^{m_1}_{l_1})/d^{N-m_1}$, which ensures that the thermodynamic state is always reached. The factor $2(W^{(m_1,m_2)}_{l_1,l_2}+W^{(m_2,m_1)}_{l_2,l_1})$ only determines the relaxation timescale. We recall that the deviation of the TD-NRG steady state and the NRG thermodynamic expectation value is usually small and within 1–10%. Therefore, the main purpose of the master Eq. (52) is to ensure the decay of the diagonal matrix elements into the thermodynamic steady state while maintaining the correct decay rate. Since the Redfield tensor decays exponentially with increasing distance $|m_1-m_2|$, we calculate $\Xi_{l_1,l_2}(m_1,m_2)$ exactly only for the tridiagonal terms $(m_1,m_2\in\{m_1-1,m_1,m_1+1\})$. For $|m_1-m_2|>1$, we replace the exact value of $X^{\tilde{m}}_{l_1,l_2}(m_1,m_2)$ in Eq. (55) by $d^{N-\max(m_1,m_2)}\delta_{Q_1,Q_2+1}$ where Q_i is the particle number of the state $|l_i,m_i\rangle$. This approximation includes the degeneration of states with the environment parameter e_i as well as the fact that only those states couple whose numbers of particles on the Wilson chain differ by one. In other words, we ignore the correct overlap matrix elements but include the proper symmetry relation between l_1 and l_2, which demands that transitions are only allowed if the states can be linked by an absorption or an emission of a particle from or into the reservoir.

4. Off-diagonal part of the density matrix

As a consequence of the secular approximation in Eq. (50), only the states of the same NRG iterations m are coupled for the ODDM. As explained above, it is highly unlikely that the same finite energy difference of the two states r,s at iteration m can be found at any other iteration m' given the energy hierarchy of the NRG approach. Then Eq. (46) simplifies to

$$\dot{\rho}^{\rm red}_{r_1,r_2}(m;t)=-\sum_{r_3,r_4}R_{r_1,r_2;r_3,r_4}(m)\rho^{\rm red}_{r_3,r_4}(m;t), \tag{77}$$

where the environment variables e_i have been traced out canceling the factor $d^{-(N-m)}$ in Eq. (51).

The ODDM has to vanish in the limit $t\to\infty$ to allow for the correct thermalization. This condition is met by the solution of Eq. (46). By definition, $1\neq 2$ and $3\neq 4$ must hold: The only possible fixed point of Eq. (77) is $\rho^{\rm red}_{r_1,r_2}(t\to\infty;m)=0$ for all $r_1\neq r_2$.

The calculation of the Bloch-Redfield tensor $R_{r_1,r_2;r_3,r_4}$ defined in Eq. (46b) involves intermediate states which run over the complete basis set of the Wilson chain. Using Eqs. (60)–(62) allows us to divide the intermediate sum over index 5 in the two first terms in Eq. (46b) into contributions from the same Wilson shell and contributions from $m'<m$ generated by 1^-_m. Neglecting the latter contributions retains the structure of the master equation for the ODDM and only leads to a slight underestimation of the relaxation rates.[2] In favor of a fast and simple implementation, we only include matrix elements of $\Xi^{\pm}_{1,2,3,4}$ where all four indices are referring to states at the same shell and used the definitions Eqs. (46c) and (46d).

5. Combined approach

In the previous sections, we derived the master equation for the reduced density matrices $\rho^{\rm red}_{s,r}(m,t)$ that will replace the time-independent reduced density matrices in Eq. (38) by our proposed hybrid TD-NRG approach,

$$\langle O(t)\rangle=\sum_{m=m_{\rm min}}^{N}\sum_{r,s}^{\rm trun}e^{it(E^m_r-E^m_s)}O^m_{r,s}\rho^{\rm red}_{s,r}(m,t), \tag{78}$$

which is the main result of this paper.

For the conservation of the trace, all reduced density matrix elements of the discarded states need to be coupled and it is crucial to maintain the symmetry of the Redfield tensor matrix elements $\Xi_{l_1,l_2}(m_1,m_2)$ in Eq. (52). At any time, the condition

$$\sum_{m=m_{\rm min}}^{N}\sum_{l}\rho^{\rm red}_{l,l}(m,t)=1 \tag{79}$$

must hold, where l only includes the discarded states at iteration m. We fulfill this requirement by solving a master equation for the diagonal matrix elements of the reduced density matrix, Eq. (52), as a first step. The off-diagonal dynamics only involves couplings within a single Wilson shell and is obtained in a second step. In a third step, the solutions for $\rho^{\rm red}_{s,r}(m,t)$ are inserted into Eq. (78), and the nonequilibrium dynamics of the quantity of interest is evaluated.

D. Algorithms for solving the master equations

The master equations Eqs. (52) and (77) are transformed into a Lindblad-style master equation that can be solved by diagonalizing the occurring nonsymmetric matrix. For a long NRG chain with a large number N_s of retained NRG eigenstates, the exact diagonalization of this nonsymmetric matrix is not possible, and we have to rely on approximate schemes. For that purpose, the biorthogonal Lanczos algorithm is utilized.

1. The Lindblad master equation

The DDM and the ODDM yield two separate equations that are solved separately. In both cases, the reduced density matrices $\rho^{\rm red}_{r,s}(m;t)$ are transformed into a supervector that contains all matrix elements. We map the diagonal matrix elements and off-diagonal density matrix elements onto equivalent vectors $\rho^{\rm red}(t)\to\vec{\rho}_{\rm DDM}(t),\vec{\rho}_{\rm ODDM}(t)$ [85] and identify the corresponding relaxation matrix. For both cases, we cast the master equations into the form

$$\dot{\vec{\rho}}(t)=-R\,\vec{\rho}(t). \tag{80}$$

[2]Note that the fixed point $\rho^{\rm red}_{r_1,r_2}(t\to\infty;m)=0$ for all $r_1\neq r_2$ remains unaltered.

For the DDM, all NRG iterations are connected, whereas in the case of the ODDM only the matrix elements of the same shells couple to each other. However, the dimension of the master equation of the ODDM comprises two NRG state indices r, s of the same iteration so the dimension of the off-diagonal vector $\vec{\rho}_{\mathrm{ODDM}}$ is $d^2N_s^2$, where N_s denotes the number of kept states a after each iteration and d the number of local DOF added in the next iteration step.

R is always a nonsymmetric matrix, and thus we have to distinguish left eigenvectors $\vec{w}_k$ and right eigenvectors $\vec{v}_k$ [44],

$$R\vec{v}_k = \lambda_k \vec{v}_k, \tag{81}$$

$$\vec{w}_k^h R = \vec{w}^h \lambda_k, \tag{82}$$

where λ_k is an eigenvalue of R. It should be stressed here that the eigenvectors $\{\vec{w}_k, \vec{v}_k\}$ constitute a biorthogonal basis, which is a consequence of the fact that the matrix R is nonsymmetric. The eigenvectors obey the biorthogonality relation $\langle \vec{w}_k, \vec{v}_{k'} \rangle = \vec{w}_k^h \vec{v}_{k'} = \delta_{k,k'}$. Note that right eigenvectors are not orthogonal to each other and $\langle \vec{w}, \vec{v} \rangle$ denotes the abstract scalar product.

The master equations can be formally solved by

$$\vec{\rho}(t) = e^{-Rt}\vec{\rho}(t=0) = \sum_{k=1}^{D} c_k e^{-\lambda_k t}\vec{v}_k, \tag{83}$$

where D is the dimension of the density matrix vector $\vec{\rho}(t)$, and the complex expansion coefficients c_k are calculated by the scalar product $c_k = \langle \vec{w}_k, \vec{\rho}(t=0) \rangle$. The supervector $\vec{\rho}(t)$ consists either of the diagonal matrix $\rho^{\mathrm{red}}_{l,l}(m;t)$ spanning all iterations $m \in [m_{\min}, N]$ or the off-diagonal matrix $\rho^{\mathrm{red}}_{r,s}(m;t)(r \neq s)$ for each iteration m and is provided by the TD-NRG algorithm. The sum over k comprises a full basis of eigenvectors of R, thus Eq. (83) is exact.

2. The biorthogonal Lanczos method

Since the matrix dimension of the Redfield tensors scale as N_s^4 and are much too large for exact diagonalization in a typical NRG framework, we have to employ a Lanczos algorithm to obtain approximate eigenvalues and—vectors in a space of reduced dimension. The Lanczos method is a diagonalization scheme that yields m approximate eigenvalues and—vectors of a given matrix, where typically $m \ll D$ holds. The biorthogonal version [44] is suited especially for non-Hermitian matrices.

In the conventional Lanczos method, the so-called Krylov subspace $\mathcal{K}_m = \{R^n\vec{\phi}_0, n \in [0, m-1]\}$ is generated by choosing a starting vector $\vec{\phi}_0$. Then, this Krylov subspace is orthogonalized by a Gram-Schmidt algorithm. By this procedure, an $m \times m$ tridiagonal matrix T_m can be generated iteratively. From the eigenvalues and eigenvectors of T_m, the corresponding Ritz values/vectors of the original matrix can be computed.

For a nonsymmetric matrix R, a corresponding left Krylov subspace $\mathcal{K}_m^L = \{\vec{\phi}_n = [R^h]^n\vec{\phi}_0, n \in [0, m-1]\}$ needs to be constructed and orthogonalization is performed between states of the left and the right space similar to co- and contravariant vectors in nonorthogonal spaces. For further details on the algorithm, the reader is referred to Yousef Saad's book [44] on iterative methods for sparse linear systems.

$\vec{\phi}_0 = \vec{\rho}(t=0)$ is chosen as a left starting vector $\vec{w}_0$ as well as a right starting vector $\vec{v}_0$ for the Lanczos method while one of them needs to be normed by $1/\langle \vec{w}_0, \vec{v}_0 \rangle$. This choice yields an accurate short-time solution for Eq. (83) which can be understood by first expanding e^{-Rt} into a Taylor series before inserting a complete eigenbasis $\sum_{k=1}^{m} |v_k\rangle \langle w_k|$ spanning the Krylov subspace. The overlap matrix elements $c_k = \langle \vec{w}_k | \rho(t=0) \rangle$ and the approximate eigenvalues λ_k obtained by the Lanczos method enter the Taylor expansion

$$\vec{\rho}(t) = \sum_{k=1}^{m}\sum_{n=0}^{m-1} \lambda_k^n |v_k\rangle\, c_k \frac{(-t)^n}{n!} + \mathcal{O}(t^m), \tag{84}$$

indicating that the accuracy increases with increasing Krylov subspace dimension m.

3. The eigenspectrum of the Bloch-Redfield tensor

Since the Bloch-Redfield tensor R in Eq. (80) is nonsymmetric, the spectrum of eigenvalues λ_k is generally complex. The master equation for the DDM, however, ensures that the eigenvalues as well as the eigenvectors are real to maintain the Hermitian property of the total density matrix. For the ODDM, all complex values can be ordered in complex-conjugated pairs.

The Lanczos approach, however, can also be used in our context to make very accurate predictions on the long-time behavior. In general, the true eigenvalues λ_k of the tensor R for the ODDM are finite and $\mathrm{Re}\lambda_k > 0$. If the Lanczos approach maintains the condition $\mathrm{Re}\lambda_k > 0$ even the approximative solution in a reduced $m \times m$ space yields a complete decay of the ODDM with possibly slightly modified relaxation timescales.

As discussed above, the tensor R for the DDM has one eigenvalue $\lambda_0 = 0$ with the corresponding right steady-state eigenvector $\vec{v}_0$. Thus, the steady-state density matrix $\vec{\rho}(t \to \infty) = c_0\vec{v}_0$ is obtained by calculating the overlap between the left eigenvector $\vec{w}_0$ and the initial vector $c_0 = \langle \vec{w}_0, \vec{\rho}(t=0) \rangle$. As we have shown in Sec. III C 1, this steady-state density matrix obtained via Eq. (52) which is given by the Boltzmann distribution for a system approaching the thermal equilibrium. As long as this thermal density matrix $c_0\vec{v}_0$ has a finite overlap with the initial density matrix, $c_0 \neq 0$, this vector is always included in the Krylov subspace by construction.

We note that the correct solution for $\vec{v}_0$ with an eigenvalue $\lambda_0 = 0$ is always found with high precision by the Lanczos approach since it is an extreme eigenvalue. Therefore, the approximation for the DDM,

$$\vec{\rho}(t) = e^{-Rt}\vec{\rho}(t=0) \approx \sum_{k=1}^{m} c_k e^{-\lambda_k t}\vec{v}_k, \tag{85}$$

using the Lanczos eigenvectors $\vec{v}_k, \vec{w}_k$ and eigenvalues λ_k, includes the correct limit for $t \to \infty$. This reflects the fact that only the very large and the very small (i.e., extreme) eigenvalues in the Lanczos eigenvalue spectrum [43] are reliable representations of the true spectrum of a matrix. Therefore, the Lanczos approach has been successfully used for the calculation of ground states of finite size Hamiltonians.

E. Summary of the employed approximations to the Bloch-Refield formalism

Let us summarize the approximations used in the Bloch-Refield formalism as well as the additional approximations performed by us whose implications we discuss in the result section below.

The Bloch-Redfield approach [24] assumes a weak coupling to the reservoir, ignores the back action of the system onto the reservoirs and the effect of the reservoirs onto the system is treated preturbatively up to second order in the system-reservoir couplings. The reservoir correlation functions are assumed to decay fast compared to the change of the reduced density matrix leading to a Markovian approximation of the time integration. As a consequence of the Markovian approximation, the real-time dynamics is predicted to be a superposition of exponential solutions, see Eq. (83). Therefore, the short-time dynamics always contain contributions linear in the time t, although the exact solution for $t \to 0$ starts with a term proportional to t^2 as demonstrated in the Appendixes. The secular approximation neglects fast oscillatory terms [24] and leads to coupled differential equations that are very similar to the Lindblad approach.

Since the Bloch-Redfield approach leads to decoupled differential equations for the diagonal and the non-diagonal matrix elements, we investigated the nature of the Redfield tensor for these two cases separately. Within the secular approximation [24], the dynamics of off-diagonal matrix elements decouples between the different NRG iterations: we can solve the differential equations separately for all Wilson shells m. We also use the simplification $\langle r, e; m| \rho_S(t) |s, e'; m\rangle \approx \rho^{\rm red}_{r,s}(m;t)\delta_{e,e'}d^{-(N-m)}$ that strictly holds only in equilibrium [53]. The dynamics of all Bloch-Redfield differential equations are solved via a biorthogonal Lanczos approach [44].

However, all diagonal matrix elements of all shells are coupled via the Redfield tensor. Since we have proven that intershell matrix elements of the Redfield tensor scale as $d^{-|m_1-m_2|}$, we only calculate the matrix elements for $|m_1 - m_2| = 0, 1$ exactly and replace the other intershell Redfield tensor elements by a constant times $d^{-\max(m_1,m_2)}$.

To benchmark the approach, we discuss the the effect of further approximations in the benchmark section, Sec IV A. Here we neglect all intershell matrix elements of the Redfield tensor, so the diagonal part of the differential equation can be solved for each Wilson shell separately. Alternatively, we only include intershell matrix elements for $|m_1 - m_2| = 0, 1$ exactly and neglect the other intershell matrix elements.

IV. BENCHMARK

A. The resonant-level model

Since the exact solution of the local dynamics in the RLM is known [51], we will use it to benchmark our hybrid NRG approach. Throughout this paper, a symmetric box density of states $\rho(\epsilon) = \rho_0\Theta(D - |\epsilon|)$ is used in all TD-NRG calculations.

The Hamiltonian of the RLM describes the hybridization of a localized level at the energy E_d with a conduction band

$$H = E_d(t)d^\dagger d + \sum_k \epsilon_k c_k^\dagger c_k + V\sum_k \{d^\dagger c_k + c_k^\dagger d\}, \quad (86)$$

where $c_k^\dagger$ creates a spinless conduction electron with momentum k and energy ϵ_k and $d^\dagger$ creates an electron on the localized level. We also allow for a time dependency of the single-particle energy $E_d(t)$. Here $\Gamma_0 = \pi\rho_0 V^2$ is the hybridization width and ρ_0 is the conduction-electron density of states at the Fermi energy.

To adapt the RLM to our hybrid approach, we set $H_{\rm imp} = E_d(t)d^\dagger d$ in Eq. (1), and H_I is given by Eq. (3). Since the number of bath flavors $M = 1$, we drop the index ν in the following.

B. Real-time dynamics

Choosing $\hat{n}_d = d^\dagger d$ as the observable $\hat{O}$ in Eq. (78), we consider a stepwise change in the energy of the level: $E_d(t) = \Theta(-t)E_d^i + \Theta(t)E_d^f$. In the wide-band limit, $(D \gg \Gamma_0)$ $n_d(t) = \langle \hat{n}_d(t)\rangle$ can be solved exactly in closed analytical form using the Keldysh formalism [51]. For $T = 0$, the analytic solution features an exponential decay from the initial equilibrium occupancy of $\mathcal{H}_i$ to the new equilibrium occupancy of $\mathcal{H}_f$ with two decay rates Γ_0 and $2\Gamma_0$.

We present data for a sudden level quench in the RLM that leads to a depletion of charge on the impurity in Fig. 7. The real-time dynamics of the local orbital occupancy $n_{\rm d}(t)$ (solid lines) are obtained with our hybrid open chain (OC) approach, Eq. (78): The constant reduced density matrix $\rho^{\rm red}_{s,r}(m)$ was made time dependent, and its dynamics was calculated by the Bloch-Redfield master equations. The master equations were solved via a biorthogonal Lanczos algorithm [44]. The dimension of the Krylov subspace for calculating the real-time dynamics of the diagonal matrix elements was set to $m = 1000$, while a Krylov subspace dimension of $m = 100$ turned out to be sufficient for obtaining the dynamics of off-diagonal matrix elements that only require coupling matrix elements within a single Wilson shell. We also supplied the exact analytic solution [51] as a black dashed line to the panels. $n_{\rm d}(t)$ was calculated for three different Wilson chain lengths N by varying the NRG parameter Λ to ensure the same target temperature $T = 0.01\Gamma_0$.

For comparison, we added the results obtained by the closed chain (CC) TD-NRG approach [51,51] for the same parameters as dotted lines of the same color. The arrow marks the thermodynamic expectation value of the equilibrium NRG using the finial Hamiltonian $\mathcal{H}_f$. We z averaged the dynamics using $N_z = 4$ different NRG chain representations [50,51,86]. The z averaging significantly reduces the finite-size oscillations but the charge occupation in the CC results still does not converge to the thermodynamic limit as expected from the exact continuum limit.

The NRG and the quench parameters are chosen close to Fig. 1(a) of Ref. [59] to make a connection to the literature. Usually, the averaged TD-NRG steady-state long-time limit is close to the thermodynamic NRG expectation value. These quench parameters, however, are deliberately chosen such that the deviation is large due to back reflections along the NRG chain as discussed in Ref. [59].

For short timescales, the TD-NRG and our OC approach track the exact result very accurately. The differences between the approaches become pronounced in the long-time limit plotted in Fig. 7(b) illustrating the influence of the NRG

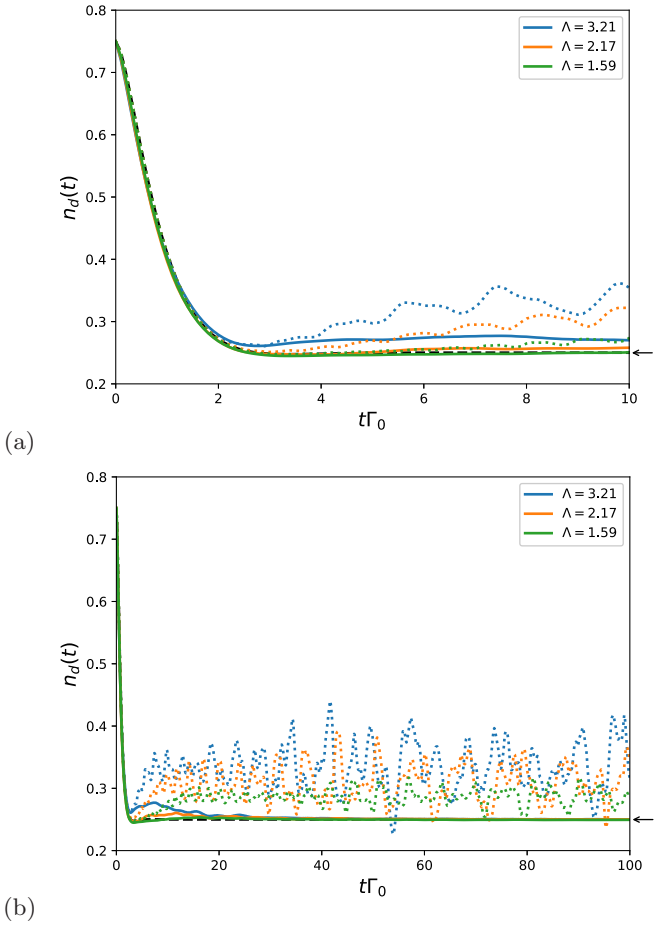

FIG. 7. Real-time dynamics of the local orbital occupancy $n_{\rm d}(t)$ (a) for a short timescale and (b) for long timescales obtained by the open-chain approach and shown as full lines compared to the TD-NRG approach which is added as a dotted line in the same color for the RLM. The exact analytical solution of Ref. [51] has been added as black dotted lines. Data for different discretization parameters Λ are presented for a sudden change in the energy of the level from $E_d^i = -\Gamma_0$ to $E_d^f = \Gamma_0$. The Wilson chain length N ($\Lambda = 1.59, N = 50$; $\Lambda = 2.17, N = 30$; $\Lambda = 3.21, N = 20$) was adjusted such that the same temperature $T = 0.01\Gamma_0$ is reached for all curves; the corresponding values for Λ are stated in the legend. NRG parameters used: $D = 10^3\Gamma_0$, $N_{\rm S} = 10^3$, $N_z = 4$.

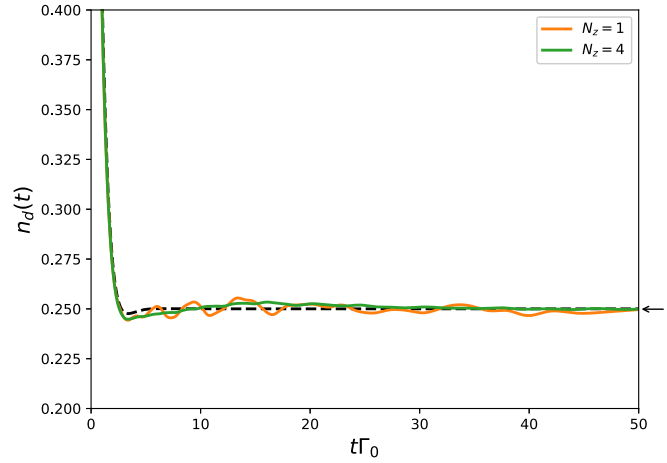

FIG. 8. Real-time dynamics of the local orbital occupancy $n_{\rm d}(t)$ for $N = 50$ with (green) and without (orange) z averaging [51]. N_z accounts for the number of different values used for the z averaging. All other parameters as in Fig. 7.

parameter Λ onto the real-time dynamics. It is well understood [59,87] that the exponential decay of the tight-binding parameters of the Wilson chain leads to a tsunami effect [87] of a severe slowdown of charge transport along the chain: The charge transport velocity mismatch leads to back reflections that increase with increasing Λ and are the origin of the deviation between the calculated real-time dynamics and the exact analytical solution. This problem is solved by including the additional reservoirs perturbatively in the dynamics. The thermal state is reproduced as a steady state in all cases with the largest deviations at intermediate times for the largest value of Λ. In this case, the TD-NRG shows the largest deviations as well. Furthermore, the bath couplings are the largest in this case so the second-order perturbation theory treating the reservoirs is insufficient to fully reproduce the exact solution. However, Fig. 7(b) clearly demonstrates the convergence for $\Lambda \to 1^+$: the choice of $\Lambda = 1.59$ already excellently tracks the exact analytic solution for the continuum problem.

The plots in Fig. 7 present the very good agreement of our proposed hybrid TD-NRG approach with the exact analytical result in the long-time limit. The OC approach provides an efficient mechanism for particle exchange with the additional reservoirs such that charge conservation is maintained in the coupled system but excess charge is balanced by the infinitely large reservoirs that couple to each chain site.

The effect of the z averaging [50,51,86] is illustrated in Fig. 8. The $N_z = 4$ result of Fig. 7 for the Wilson chain of length $N = 50$ (green) is plotted in comparison to the data without z averaging ($N_z = 1$, orange curve). The discrepancy between the different data obtained from the OC approach is small: The z averaging evens out the finite size oscillations which are very close to the exact solutions plotted as a black dashed line. The hybrid approach perfectly reproduces the thermal value of the occupation as indicated by the black arrow at the right side of the figure and follows the exact solution very accurately.

An important component of our hybrid approach is the coupling of the reduced density matrix elements between all Wilson shells. Since the calculation of all Bloch-Redfield tensor elements are in principle possible—see Sec. III C 2—but numerically too expensive for a practicable implementation, we only calculate the shell diagonal tensor matrix elements and those between adjacent shells $m' = m \pm 1$ in a complete manner. For the coupling of iterations with $|m_1 - m_2| > 1$, we use the approximation $X^{\tilde{m}}_{l_1,l_2}(m_1, m_2) \to d^{N-\max(m_1,m_2)}\delta_{Q_1,Q_2+1}$ as introduced in Sec. III C 3.

The effect of different approximations to the Bloch-Redfield tensor is depicted in Fig. 9. We augmented the OC approach data for $N = 50$ taken from Fig. 7 with the results obtained with additional approximations in calculations of diagonal density matrix elements.

The blue curve (no shell coupling) is obtained by a tensor $\Xi_{l_1,l_2}(m_1, m_2)$ that is diagonal in the Wilson shell indices,

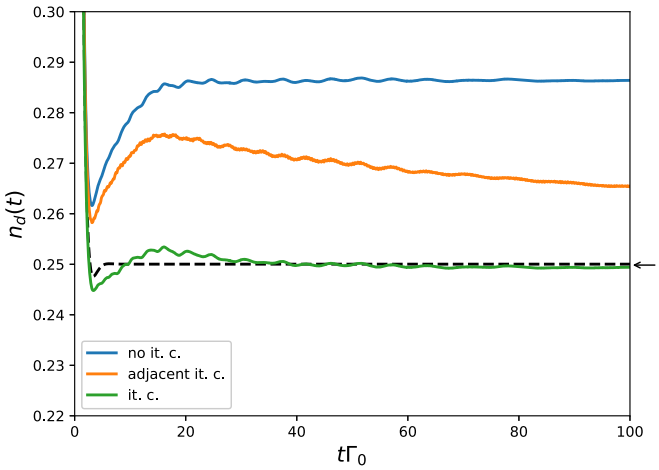

FIG. 9. Impurity occupancy $n_d(t)$ obtained by the full open chain hybrid approach, i.e., with a coupling of all NRG iterations (green) by an adjacent approximation for $\Xi_{l_1,l_2}(m_1,m_2)$ including $m_1 = m_2$ and $m_1 = m_2 \pm 1$ (orange) and restricting to $m_1 = m_2$, i.e., with no coupling between discarded states of different NRG iterations (blue). NRG parameters as in Fig. 7 for $N = 50$.

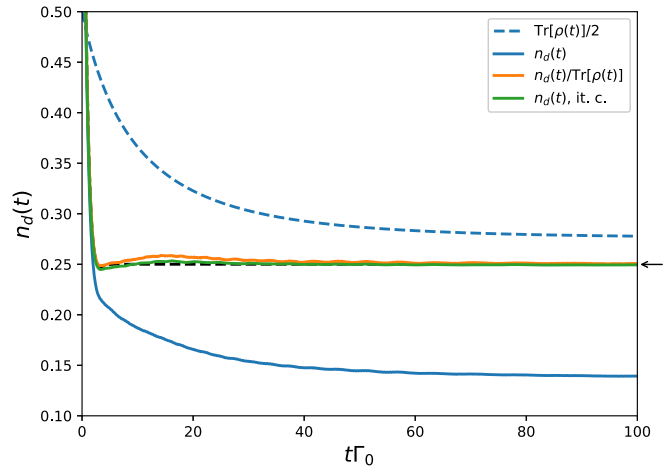

FIG. 10. Impurity occupancy $n_d(t)$ obtained by the OC hybrid approach but with different approximations. The green curve is obtained by the full algorithm (all discarded states are coupled) and is taken from Fig. 7. For the blue curve, we neglected the coupling between discarded states of different iterations and included the relaxation into the kept states for each iteration instead. The loss of the trace Tr[$\rho(t)$] of the density matrix as a function of time is shown as a blue dashed line. Normalizing the blue curve by the time dependent trace yields the orange curve. NRG parameters as in Fig. 7 for $N = 50$.

i.e., $\Xi_{l_1,l_2}(m_1,m_2) = \delta_{m_1,m_2}\Xi_{l_1,l_2}(m_1,m_1)$. The coupling of the additional reservoirs generates a damping in the real-time dynamics of the orbital occupancy $n_d(t)$. Since the sum of the diagonal density matrix elements remains conserved in each Wilson shell as in the TD-NRG, the steady-state value is very similar to the time-averaged TD-NRG value at infinitely long times: The decay into the thermal steady-state is not possible without coupling the discarded states of different iterations m.

Note that even though the approximation $\Xi_{l_1,l_2}(m_1,m_2) \propto \delta_{m_1,m_2}$ conserves the trace, it does not reach the correct thermal steady state. The reason for this is that for completely decoupled shells, the Bloch-Redfield equations feature a nonphysical conservation of each contribution to the trace within each energy shell. As a consequence, a correct relaxation into the thermal equilibrium characterized by the detailed balance condition [see also Eq. (57)]

$$\lim_{t\to\infty} \frac{\rho^{\mathrm{red}}_{l_1,l_1}(t;m_1)}{\rho^{\mathrm{red}}_{l_2,l_2}(t;m_2)} = d^{m_2-m_1} e^{-\beta(E^{m_1}_{l_1}-E^{m_2}_{l_2})} \tag{87}$$

not possible.

This is fundamentally changed when the adjacent approximation which includes all tensor elements $m_1 = m_2 \pm 1$ is applied (depicted as an orange line). We notice a decay of $n_d(t)$ at intermediate times even though there is no convergence on the timescales plotted in Fig. 9. However, we proved analytically in Appendix (B10) as well as numerically—not shown here—that the thermal expectation value of n_d with respect to H_f is already obtained as the steady-state value in this approximation. The decay rate, however, is very low. This problem is solved by our approximate treatment of all other matrix elements $\Xi_{l_1,l_2}(m_1,m_2)$ that includes a coupling of the diagonal density matrix elements of all Wilson shells with exponentially decaying matrix elements that are allowed by the symmetry but ignoring the precise values of the overlap matrix elements (green curve).

In Fig. 10, we plot the all-coupling approach (green) versus a complete separation of the iterations (blue), comparable to the blue curve in Fig. 9. The difference lies in the fact that we now include all states, discarded and kept, at all iterations for the independent Bloch-Redfield equations. This implies a realistic relaxation of the high-energy states into the low-energy kept states for each NRG iteration. Since the kept states of the diagonal part of the density matrix, however, are not included in Eq. (78), we end up with an effective unphysical loss of the trace. This can easily be compensated for by artificially dividing any nonequilibrium expectation value by the time-dependent trace and thus ensuring to keep the trace of the resulting expression constant (orange curve). That way, a correct thermalization can be realized. Even though this approximation is very efficient regarding computation time and memory requirements, its motivation is unphysical. For that reason, we will continue this paper by using the approach that couples all iterations and thus includes an inherent conservation of the trace.

C. Computational time considerations

The TD-NRG, the CC algorithm, comprises a standard NRG run and a backward iteration for the real-time dynamics by tracing out the reduced density matrix for each iteration that is needed as an initial condition for the time-dependent reduced density matrix [50,51]. The limiting factor is the number of time points that should be evaluated for each expectation value. The TD-NRG run takes three to ten times longer than the underlying NRG itself.

The first OC part is the final forward run. Here the runtime is determined by building the correlation functions $C_m(\omega)$ to then build the Bloch-Redfield tensors R [see Eq. (46)].

This procedure scales $\propto N_S^2 N^2$ since for each iteration m at least the same number of individual tensors has to be build within our approximation. Next is the construction and diagonalization of the tensor that connects all NRG iterations for the diagonal part of the density matrix. Here the Lanczos depth $m_{\text{lan, diag}}$ (equivalent to the Krylov space dimension) is the limiting factor. For large values of Λ and long chains, very small effective temperatures are reached, which means that the tensor has to cover a broad energy spectrum. Hence, for a sufficient resolution to resolve the long-time dynamics, a larger value for $m_{\text{lan, diag}}$ has to be chosen accordingly. For $T = 0.01\Gamma_0$, we have chosen $m_{\text{lan, diag}} = 1000$. The last part of the program is the backward run where the Bloch-Redfield tensor for the off-diagonal dynamics of each iteration is diagonalized and then its contribution to the complete expectation value is calculated for each individual time t. Since those tensors only contain one shell, they are significantly smaller and thus a Lanczos depth of $m_{\text{lan, off-diag}} = 100$ is sufficient. The latter two sections of the program roughly scale linearly with the chain length N.

The $N = 20$ curve of Fig. 7, for instance, required a total runtime of 78 min on an Intel Xeon 12 core workstation which is distributed roughly by 50% on the building of the tensors. Here we have parallelized with ten threads for the value $\tilde{m}$ in Eq. (46c). The backward run and the TD-NRG portion are parallelized for the single subspaces on each iteration and the former takes a runtime percentage of 35% while the mere TD-NRG takes less than 1%. The building and diagonalization of the Bloch-Redfield tensor for the diagonal part of the density matrix requires the remaining runtime, which lies around 14%. We did not implement the parallelization of the Lanczos algorithm. When z averaging was utilized, an independent thread can be used for each z value which enables a simple parallelization of almost the entire program.

V. REAL-TIME DYNAMICS FOR CORRELATED MODELS USING THE OPEN-CHAIN APPROACH

After establishing the quality of the OC algorithm to the nonequilibrium dynamics by comparing the results of the approach to the exact analytical solution of the occupancy dynamics in the RLM, we apply our approach to two problems for which an exact analytic solution is unknown: the interacting RLM and the SIAM.

A. Interacting resonant-level model

To proceed to the first nontrivial problem of this paper, the RLM is extended by a Coulomb repulsion U between the local impurity level and the band which defines the interacting resonant level model (IRLM). Here the modified impurity Hamiltonian H_{imp} reads

$$H_{\text{imp}} = E_d(t) d^\dagger d + U\left(d^\dagger d - \tfrac{1}{2}\right)\left(f_0^\dagger f_0 - \tfrac{1}{2}\right). \tag{88}$$

This model has been intensively studied [66,67] in the 1970s due to its connection to the Kondo problem [88]. In recent years, the interest has shifted to its nonequilibrium properties, particularly for a biased two-lead setting [30,31,89,90].

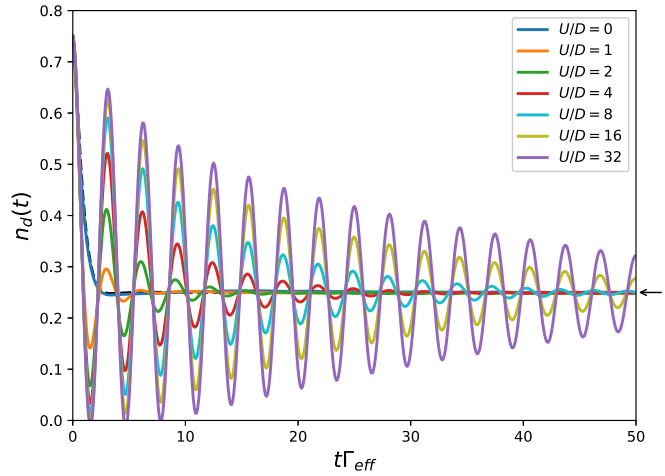

FIG. 11. The real-time dynamics of $n_d(t)$ vs time in the IRLM for different values of U obtained by the open-chain hybrid approach (solid lines) for a sudden change in the energy of the level from $E_d^i/\Gamma_{\text{eff}} = -1$ to $E_d^f/\Gamma_{\text{eff}} = 1$. The analytical $U = 0$ result is added as a guidance (black dashed line). The thermodynamic expectation value n_d^f is added as a black arrow on the r.h.s of the figure for comparison. NRG parameters: $\Lambda = 1.59, N = 50, D/\Gamma_{\text{eff}} = 10^3, N_S = 10^3, N_z = 4$ so $T/\Gamma_{\text{eff}} = 0.01$.

The IRLM shares the line of low-energy fixed points with the noninteracting RLM after renormalization of

$$\Gamma_0 \to \Gamma_{\text{eff}} \approx D(\Gamma/D)^{1/(1+\alpha)}, \tag{89}$$

with $\alpha = 2\delta - \delta^2$ and $\delta = (2/\pi)\arctan(\pi\rho U/2)$. Nevertheless, the nonequilibrium dynamics of both models differs significantly [59,60]. While the coherent oscillations present in the analytic solution [51] are strongly damped in the RLM and, therefore, are only observable for extreme parameter choices, an increasing number of coherent oscillations in $n_d(t)$ is found with increasing U [59,60] in the IRLM. The additional Coulomb repulsion U favors the single-electron subspace spanned by the impurity orbital and the first Wilson chain site. The coherent oscillation frequency is given by the energy difference between the binding and antibinding molecular state formed by the hybridization since the initial configuration can be expanded into these two local states with different eigenenergies. In the limit of large U, the rest of the Wilson chain is essentially decoupled from those two states, and the virtual charge fluctuations between these states and the rest of the Wilson chain induces a damping of these coherent oscillations that is proportional to U^{-2} [60].

To ensure quenches between the same initial and final equilibrium fixed points, the hybridization strength Γ_0 has been adjusted such that $n_d(0) = 0.75$ and $n_d(\infty) = 0.25$ for all values of U, implying $E_d^i/\Gamma_{\text{eff}} = -1$ and $E_d^f/\Gamma_{\text{eff}} = 1$ for all curves. The OC results for the local occupancy $n_d(t)$ are shown in Fig. 11. Upon increasing U, a new timescale τ_U emerges which is much larger than the thermodynamical relaxation timescale $\tau_0 \propto 1/\Gamma_{\text{eff}}$. The timescale τ_U characterizes the decay of the amplitude of coherent oscillations. For $U \to \infty$, the charge simply oscillates between the impurity and the first Wilson chain site, while for a finite U the

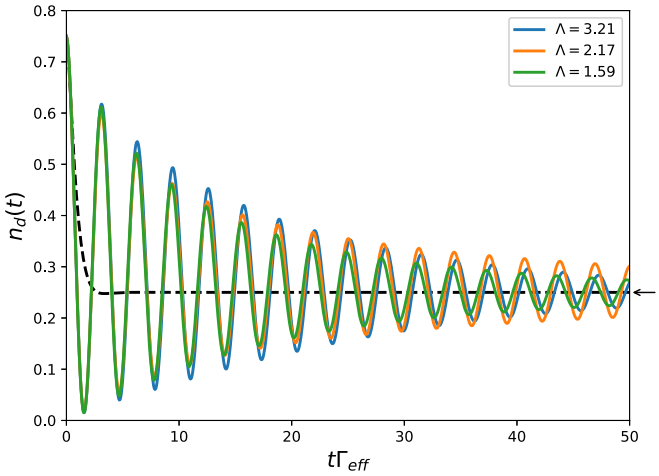

FIG. 12. The real-time dynamics of $n_d(t)$ vs time in the IRLM for a fixed $U/D = 16$ but different chain length N and NRG discretization parameter Λ combinations. The NRG parameter Λ ($\Lambda = 1.59, N = 50$; $\Lambda = 2.17, N = 30$; $\Lambda = 3.21, N = 20$) was adjusted such that the same temperature $T = 0.01\Gamma_{\rm eff}$ is reached for all curves and $N_S = 300$. The analytical $U = 0$ curve is added as a dashed line for illustration purposes.

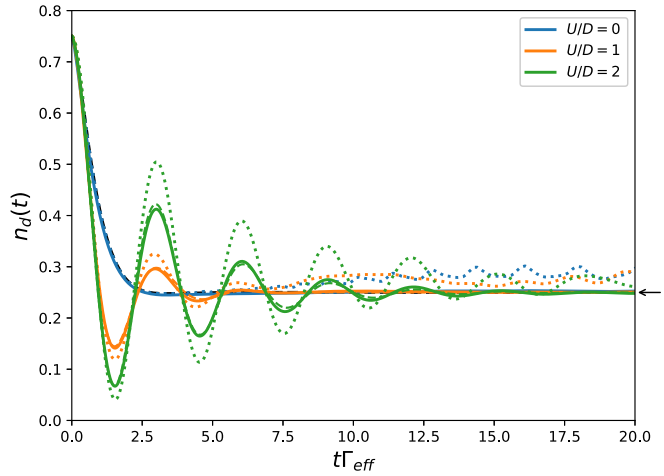

FIG. 13. The real-time dynamics of $n_d(t)$ vs time in the IRLM for different values of U obtained by our OC hybrid approach (solid lines) and by the TD-NRG (dotted line) in the same color as well as a fit to Fermi's golden rule (dashed line). NRG parameters as in Fig. 7.

oscillations are damped and the system approaches thermal equilibrium.

Since the partitioning of the original continuum depends on the NRG discretiation parameter Λ, we investigated the nonequilibrium dynamics of $n_d(t)$ for a fixed value of $U/D = 16$ and the same local quench parameters as used in Fig. 11 but for three different values of Λ. The corresponding chain lengths are adjusted such that the effective temperature is the same for all three cases. The results are plotted in Fig. 12. Remarkably little effect of Λ on the oscillation frequency and the relaxation time is found, although Λ strongly influences the spectral weight of the coupling to the additional reservoirs. This indicates that our OC approach is rather robust and the results depend only weakly on the discretization parameter.

The difference of our approach and the TD-NRG in the IRLM is illustrated for a few small values of U in Fig. 13. Although the oscillation frequency is the same as reported by Güttge *et al.* [60], we note that the decay time τ_U of the OC approach is shorter than predicted by the CC approach. The analytical golden rule estimate of Ref. [60] is based on a CC topology, where the impurity orbital and the first Wilson chain site ($m = 0$) only couple via the hopping parameter t_0 to the rest of the system. The Fermi's golden rule calculation treats the first two orbitals as a closed system and adds a perturbative coupling to the rest of the chain. The long-time artifacts of the CC approach are suppressed in Ref. [60] by combining the TD-NRG with a TD-DMRG approach for a very long tight-binding chain and stopping the simulation before reflections at the chain end are detectable at the impurity. In our approach, the additional reservoirs cause an additional decay of the coherent oscillations and ensure the thermalization to the expectation value.

In Fig. 14, we present a comparison of numerically extracted parameters with their analytical predictions. In the top panel, we show the NRG results for the ratio $\Gamma_0/\Gamma_{\rm eff}$ as a solid line, Γ_0 being the bare hybridization strength of the model. The results of the perturbative RG prediction according to Eq. (89) have been added as a dotted line. Both graphs agree excellently in the limit of large U. The middle panel and the bottom panel of Fig. 14 present the numerical fit to the analytical golden rule results stated in Eq. (17) of Ref. [60] and their analytical predictions. The oscillation frequency Ω of the occupation was calculated by $\Omega = \epsilon_+ - \epsilon_- = 2\sqrt{(E_d/2)^2 + (V_{\rm eff})^2}$ with $V_{\rm eff}$ being the renormalized hybridization strength parametrizing $\Gamma_{\rm eff} = \pi V_{\rm eff}^2/2D$.

As expected, the analytical prediction agrees very well with the numerical value for the large U regime where the golden rule result is applicable. Nevertheless, a significant deviation between the analytical and the numerically extracted relaxation time τ is observed. The analytical solution

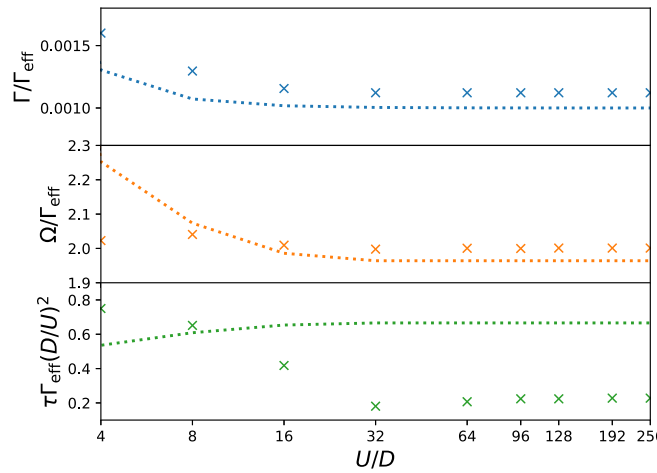

FIG. 14. A comparison of analytical estimates (dotted lines) and the numerical values (stars) for three different IRLM parameters. The coupling strength U/D has been varied.

presented in Ref. [60] predicts

$$\tau\Gamma_{\rm eff}\left(\frac{D}{U}\right)^2 = \frac{\pi^4}{256}\frac{\Omega}{D}\frac{\Gamma_{\rm eff}}{\Gamma} \tag{90}$$

and is plotted as a dotted green line in the bottom panel of Fig. 14. As mentioned above regarding Fig. 13, the relaxation time extracted for the OC in the IRLM does not exactly match the golden rule prediction. In fact, we approximately obtain an overlay of three different decay times, the smallest one stemming from the DDM. The remaining two decay times damp the oscillations as exponential functions in Eq. (78). The largest decay time influences the long-time behavior of the occupation and thus we have chosen this value to be plotted in comparison to the golden rule approximation for τ in Fig. 14. Obviously, the long-time relaxation $\tau \propto (U/D)^2$, as predicted in the golden rule, whereas the asymptotic value for large U is smaller, thus implying a faster relaxation, as discussed above.

In the OC approach, presented here, the fundamental difference to the CC approach is the direct coupling of an auxiliary reservoir to the first Wilson site $m = 0$ as well: Even if we artificially decouple the rest of the Wilson chain from the first site by setting $t_0 = 0$, the oscillations remain damped for any finite U due to the relaxation channel provided by the first bath. In the limit of large U, we expect a superposition of two damping channels: damping by the rest chain and damping by the high-energy modes of the reservoir $\Delta_0(z)$. This additional damping mechanism in our OC explains the decrease of τ_U compared to the CC approach as demonstrated in Fig. 13. Our OC also avoids the reflections of charge waves propagating along the Wilson chain since they are damped by the reservoirs as expected from the continuum problem. Furthermore, the analysis of the RLM has already shown that the relaxation times of our approach are slightly exaggerated for $t\Gamma_0 < 10$ (see, e.g., Fig. 9), which stems from the approximation in Sec. III C 3 where the matrix elements of the Bloch-Redfield tensor for $|m - m'| > 1$ are still assumed slightly too large. This yields a faster relaxation for short times fading into a smaller rate for later times.

B. Single-impurity Anderson model

1. Definition of the model

In the SIAM, the spin degree of freedom $\nu = \sigma$, the on-site repulsion U, and an optional local magnetic field strength $b(t)$ are added to the RLM. The SIAM impurity Hamiltonian now reads

$$H_{\rm imp} = \sum_\sigma \left[E_d(t) - \frac{\sigma}{2}b(t)\right]d_\sigma^\dagger d_\sigma + U d_\uparrow^\dagger d_\uparrow d_\downarrow^\dagger d_\downarrow. \tag{91}$$

We choose the spin quantization axis parallel to the external magnetic field direction and absorb the prefactor $g\mu_B$ into the magnetic field strength b which is consequently measured in the units of energy. Since we are not interested in the limit of large magnetic fields of the order of the band width [91], we neglect the small corrections due to the spin polarization of the conduction band and only apply a local magnetic field for simplicity. The bath Hamiltonian and the interaction Hamiltonian are given by Eqs. (32) and (34), respectively, where the spin index σ is summed over $M = 2$ values.

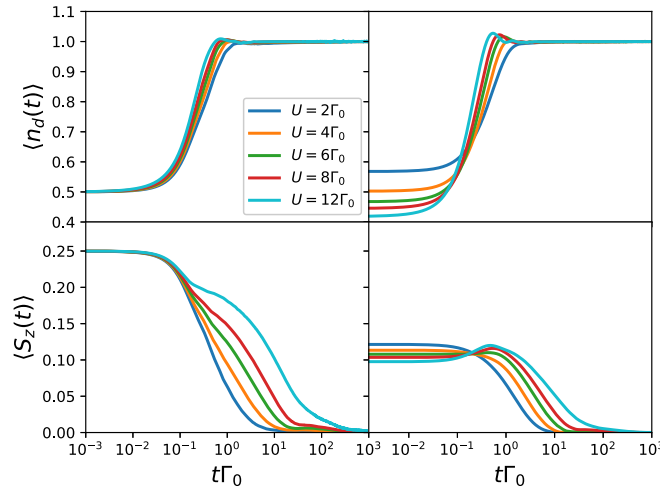

FIG. 15. Impurity occupancy $n_d(t)$ and spin polarization $S_z(t)$ vs time after the quench on a logarithmic timescale. The upper and lower right panels show the results of scenario (i) leaving the hybridization strength constant. In the upper and lower left panels, the data after switching the hybridization strength on at $t = 0$ are plotted. Parameters: $\Lambda = 1.66$, $D = 20\Gamma_0$, $N = 30$, $T = 0.01\Gamma_0$, $N_z = 4$, $N_S = 10^3$.

2. Real-time spin and charge dynamics

We apply an instantaneous quench by a change of the parameters $E_d^i \to E_d^f$, $b_i \to b_f$, and $\Gamma_i \to \Gamma_f = \Gamma_0$ at $t = 0$. Since the hybridization strength $\Gamma_f = \Gamma_0$ is the same in all cases, all energies are given in units of Γ_0.

We investigated two different quench scenarios: We either (i) keep the impurity hybridization constant, i.e., $\Gamma_i = \Gamma_f$ or (ii) we switch on the hybridization at $t = 0$. The initial low-energy fixed points of both scenarios are fundamentally different. The first case corresponds to the conventional low-energy fixed points of the SIAM [58] for the parameter choice of U, E_d, and b, while in the second scenario we start from the unstable local moment fixed point where the impurity is decoupled from the conduction band continuum.

In both cases, we leave U constant and only quench E_d and the magnetic field b. Initially, we set $b_i = \Gamma_0$ to induce a spin polarization and switch off the magnetic field at $t = 0$. We also start with a degeneracy of the spin-up impurity state and the unoccupied state by setting $E_d^i - b_i/2 = 0$. For scenario (ii), the spin-down state is initially completely depopulated so $n_d(0) = 0.5$, and the local spin polarization S_z is fixed to $S_z(0) = 1/4$. For scenario (i), the initial occupation and spin polarization depend on the ratio U/Γ_0.

At $t = 0$, we quench the level position to $E_d^f = -U/2$ and switch off the magnetic field, $b_f = 0$. Therefore, the thermodynamic low-energy fixed point of H_f is the same for all values of U and both scenarios: the particle-hole symmetric strong coupling fixed point.

In Fig. 15, the dynamics of the impurity occupancy $n_d(t)$,

$$n_d(t) = \langle d_\uparrow^\dagger d_\uparrow + d_\downarrow^\dagger d_\downarrow\rangle(t),$$

and the dynamics of the spin polarization $S_z(t)$,

$$S_z(t) = \tfrac{1}{2}\langle d_\uparrow^\dagger d_\uparrow - d_\downarrow^\dagger d_\downarrow\rangle(t),$$

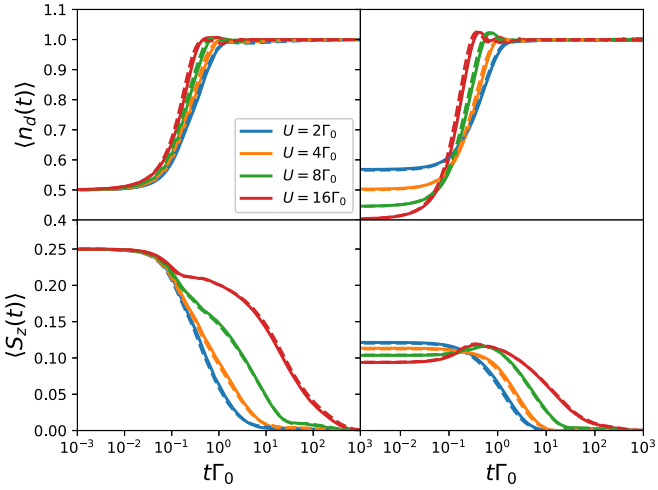

FIG. 16. Comparison of $N_S = 300$ (dashed lines) to $N_S = 1000$ (solid lines) different states for the SIAM regarding the impurity occupation $n_d(t)$ and the spin polarization $S_z(t)$.

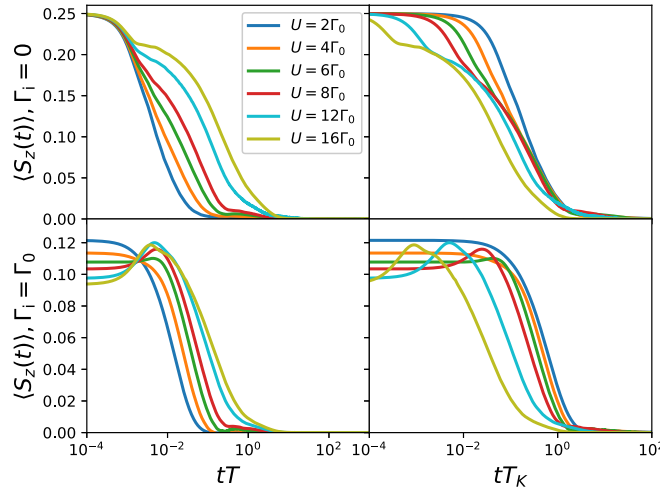

FIG. 17. $S_z(t)$ data taken from Fig. 15 for $\Gamma_i = 0$ at the top and $\Gamma_i = \Gamma_0$ at the bottom. The time is scaled by the system temperature T on the left and by the respective Kondo temperature T_K (which depends on U) on the right.

are plotted as a function of time. The data for five different values of U are shown using our hybrid OC approach.

Since the number of states increases by a factor of 4 in each NRG iteration, 3/4 of the states are discarded at the end of each iteration in the NRG algorithm. Hence, the number of matrix elements of the Bloch-Redfield tensors is substantially larger than in the RLM case and the numerical costs of the Lanczos approach for coupling the diagonal density matrix elements become very high. While the standard TD-NRG requires around two minutes on today's desktop computers, the OC approach for each of the curves presented in Fig. 15 took about three days on a workstation node utilizing all 16 cores.

The effect of choosing different numbers of kept states N_S after each NRG iteration is demonstrated for the SIAM in Fig. 16. We supplement the data for Fig. 15 shown as solid lines with $N_S = 300$ states (dashed lines) for the same quench parameters. Obviously, the differences are very small, suggesting the choice of $N_S = 1000$ states to be perfectly sufficient for our purpose.

The charge relaxation and the spin relaxation occur on different timescales [50], as can already be seen in Fig. 15. While the charge relaxation occurs on the scale set by $\Gamma_f = \Gamma_0$, the spin decay time shows significant U dependency. The equilibrium energy scale that governs the crossover from the local moment fixed point into the strong coupling fixed point is the Kondo temperature T_K. This parameter is a measure for the temperature at which the local magnetic moment is already 70% screened [64].

To investigate the spin dynamics in more detail, we plotted the $S_z(t)$ data shown in Fig. 15 versus the dimensionless times tT and tT_K in Fig. 17, where T is the system temperature. For scenario (ii)—top right panel—we find a very good universality of the long-time behavior of $S_z(t)$. This scenario starts from the local moment fixed point with a decoupled impurity and approaches the symmetric strong coupling fixed point and, therefore, partially tracks a thermodynamic flow. The dynamics is clearly governed by the Kondo scale for large Kondo temperatures where $T \ll T_K$. The long-time tails of the $U/\Gamma_0 = 2, 4, 5, 8$ curves show universality. Since $T_K(U/\Gamma_0 = 8) = 0.046\Gamma_0$, we start to see deviations since the temperature is $T/\Gamma_0 = 0.01$ in all simulations. For $U = 16\Gamma_0$, the system temperature $T \approx 4.2T_K$ is clearly above the Kondo temperature. The top left panel of Fig. 15 suggests that the relevant decay scale is set by the thermal fluctuations for $T > T_K$, as $S_z(t)$ decays on the scale of $1/T$.

For scenario (i), depicted in the two lower panels of Fig. 15, the Kondo temperature does not provide such a universal scaling. The characteristic decay time is of the order of T_K for temperatures $T \ll T_K$ but it depends on the initial preparation of the system. Upon increasing the relative temperature T/T_K, the thermal fluctuations start to dominate the decay time as in scenario (ii).

As a further indication for the correctness of the TD-NRG results, an analytic solution will be used for case (i). The dynamics of the density operator is calculated up to second order in the impurity coupling function.This solution is only valid on short timescales and becomes asymptotically exact in the limit $t \to 0$. The calculation requires a numerical evaluation at finite temperature but in the limit of $T \to 0$ we arrive at the compact analytical expression

$$n_d(t) = \tfrac{1}{2} + 2B(t, U/2), \quad S_z(t) = \tfrac{1}{4} - B(t, -U/2), \quad (92)$$

with

$$B(t,\epsilon) = \frac{\Gamma_0 t}{\pi}\,\mathrm{Si}(\omega t) + \frac{\Gamma_0}{\omega}\frac{\cos(\omega t) - 1}{\pi}\Bigg|_{\omega=-\epsilon}^{D-\epsilon}, \quad (93)$$

and $\mathrm{Si}(\epsilon)$ being the sine integral. The full calculations can be found in Appendix C.

The OC (solid line) and CC (dotted line) numerical data for the change of the time-dependent spin (orange) and charge (blue) expectation values are compared to the analytical curves (dashed lines) for $U/\Gamma_0 = 2$ and $D/\Gamma_0 = 20$ in Fig. 18. The CC (TD-NRG) agrees perfectly with the analytics for times $t\Gamma_0 < 0.1$. Here, the deviation of the OC solution from both curves is clearly visible, but this effect is exaggerated

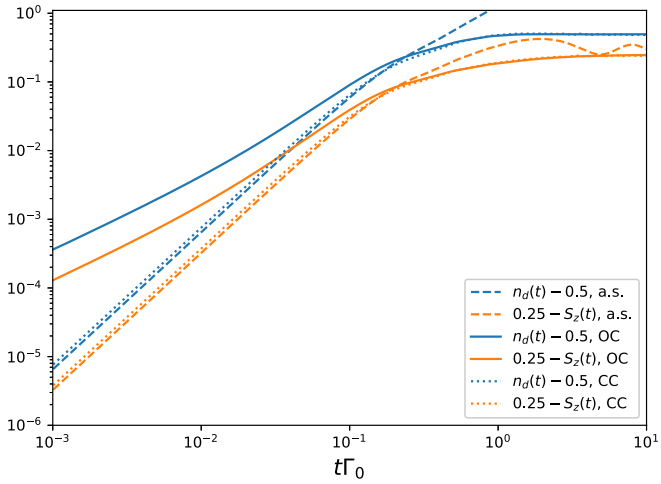

FIG. 18. Impurity occupation $n_d(t)$ and spin $S_z(t)$ of the open chain (OC) compared to the closed chain (CC, dotted) and the analytical solution (a.s., dashed) according to Eq. (92) plotted on a double logarithmic scale.

by the double logarithmic plot. The OC and the CC approach merge on timescales $0.1 < t\Gamma_0$. The initial deviations are a generic feature of the Bloch-Redfield formalism where short-time quantum correlations are ignored due to the factorisation under the integral.

VI. CONCLUSION

We presented a hybrid approach to the nonequilibrium dynamics in QISs which combines the strength of the NRG and the strength of weak coupling approaches for open quantum systems to restore the original continuum problem. The continuous fraction expansion of the coupling function between the quantum impurity and the environment yields a Hamiltonian representation of the original problem decomposed into a discrete Wilson chain and a set of high-energy additional reservoirs, each coupled to a single Wilson chain site. These reservoirs represent the high-energy modes of the original coupling function that only couple indirectly to the quantum impurity. Therefore, the standard NRG is defined as an approximation which neglects the coupling to the additional reservoirs.

A different discretized representation of a QIS augmented with a Lindblad dynamics was previously considered [41,42] in the context of nonequilibrium quantum transport. Their approach treats the Lindblad coupling tensor elements as fitting parameters that are determined by a variational approach. In our method, we are able to analytically construct the exact coupling functions to the additional reservoirs that are required to recover the original continuous coupling function of the problem.

Since the NRG has been established as an excellent tool [58] for the equilibrium problem, we propose to augment the TD-NRG with a perturbative Bloch-Redfield treatment of the coupling to the auxiliary reservoirs. We modified the standard Bloch-Redfield approach [24] derived for the full density matrix of a finite size system: The approach is applied to the set of reduced density matrices that are required for the dynamics of local observables at and around the quantum impurity to handle the huge amount of discarded states generated by the NRG truncation. The fourth-rank Bloch-Redfield tensor is evaluated exactly from the analytically constructed coupling functions to the additional reservoirs within a Wilson shell and for the coupling between the diagonal matrix elements of the density matrix of adjacent shells. We used the generic scaling properties of the matrix elements to substitute the cumbersome exact enumeration by a simplified analytical form for the tensor elements connecting states of Wilson shells that are far apart from each other. This is justified since the matrix elements decay exponentially with the shell distance $|m_1 - m_2|$ and their precise value does not affect the steady state solution of the master equation.

It turns out to be crucial that all diagonal matrix elements of the reduced density matrices of all energy shells are coupled. We have proven that the steady state of the approach is the NRG thermal equilibrium value for a hybrid system coupled to reservoirs that share a common chemical potential. A different current-carrying steady state can be achieved in a two-lead setup with different chemical potentials [41,42]. This will be the subject of a further publication.

We used the known analytic solution of the RLM [51] as a benchmark for the proposed hybrid approach and found excellent agreement between the analytical and the numerical curves. A comparison of real-time dynamics between the TD-NRG and the OC hybrid approach was presented for two nontrivial strongly correlated models: the IRLM and the SIAM. In all cases, our hybrid approach significantly reduced the finite-size oscillations as well as removing the slight deviation between the nonequilibrium steady-state expectation values and the NRG thermal equilibrium values.

Our hybrid approach has the potential to be extended in two ways: (i) adding leads with different chemical potentials and numerically calculating a current carrying steady state in the strong coupling limit and (ii) deriving a similar approach for the NRG spectral functions to remove the necessity for an artificial broadening [58] and replacing it by the physical processes included in the original continuum model prior to the discretization.

APPENDIX A: RELATION BETWEEN THE FIRST WILSON-CHAIN PARAMETER t_0 AND THE CONTINUOUS FRACTION COUPLING PARAMETER V_0

Below we will show, that the zeroth reservoir of the OC, which represents the start of our reservoir algorithm, is sufficient for a Wilson chain parameter t_0 of any $\Lambda > 1$. Inserting Eq. (16) into Eq. (17) yields

$$\pi V_0^2 = V^2 \int_{-\infty}^{\infty} d\omega \frac{\mathrm{Im}\Delta(\omega)}{\mathrm{Re}\Delta(\omega)^2 + \mathrm{Im}\Delta(\omega)^2} = \frac{2D}{\pi} \int_{-D}^{D} d\omega \frac{\pi^2}{4\mathrm{artanh}^2(\omega/D) + \pi^2} = \frac{\pi}{3} D^2. \quad \text{(A1)}$$

Since

$$t_0^2 = \frac{D^2}{4} \frac{(1-\Lambda^{-1})(1+\Lambda^{-1})^2}{1-\Lambda^{-3}}, \quad \text{(A2)}$$

the inequality $V_0 > t_0$ follows for any $\Lambda > 1$.

APPENDIX B: DERIVATION OF THE BLOCH REDFIELD APPROACH

The dynamics of the density operator $\rho_I(t)$ is governed by the differential equation

$$\partial_t \rho_I(t) = i[\rho_I(t), V_I(t)] \tag{B1}$$

in the interaction picture, where the system-reservoir coupling takes the form

$$V_I(t) = e^{iH_0 t} H_I(N) e^{-iH_0 t} \tag{B2}$$

and

$$\rho_I(t) = e^{iH_0 t} \rho(t) e^{-iH_0 t}. \tag{B3}$$

Here the operators are transformed by $H_0 = H_N^{\mathrm{NRG}} + H_{\mathrm{res}}(N)$.

For expectation values of local operators, it is sufficient to know the local density operator $\rho_S(t) = \mathrm{Tr}_R[\rho_I(t)]$ where we have traced out all the reservoir DOFs. This operator is acting only on the Wilson chain or system S, respectively.

Now Eq. (B1) can be adapted to derive a Bloch-Redfield equation for the reduced density matrix $\rho_S(t)$ by integrating the equation

$$\rho_I(t) = \rho_I(0) + i \int_0^t dt' [\rho_I(t'), V_I(t')] \tag{B4}$$

and substituting the resulting $\rho_I(t)$ back into the differential equation. The expression

$$\partial_t \rho_I(t) = i[\rho_I(0), V_I(t)] - \int_0^t dt' [[\rho_I(t'), V_I(t')], V_I(t)] \tag{B5}$$

is obtained which is used to derive the dynamics of the local density operator

$$\partial_t \rho_S(t) = -\int_0^t dt' \mathrm{Tr}_R[[[\rho_S(t')\rho_R, V_I(t')], V_I(t)]] \tag{B6}$$

after tracing out all reservoir DOFs. This operator is acting only on the DOF of the Wilson chain. The first term of the r.h.s of Eq. (B5) vanishes due to particle number conservation.

To derive the dynamics of the reduced density operator, the weak coupling approximation [24] is employed and the full density operator $\rho_I(\tau) \approx \rho_S(\tau)\rho_R$ is factorized, where ρ_R denotes the equilibrium density operator of the reservoir which remains unaltered by the coupling to the Wilson chain.

The bath coupling functions $\Gamma_{\nu m}(\epsilon)$ derived in Sec. II C enter the expression for the greater and lesser reservoir GF for each reservoir [92]. The lesser or particle GF,

$$\begin{aligned} G^<_{\nu,\tilde{m}}(t,t') &= i|t'_{\nu\tilde{m}}|^2 \mathrm{Tr}_R[\rho_R c^\dagger_{0\nu\tilde{m}}(t) c_{0\nu\tilde{m}}(t')] \\ &= i \int_{-\infty}^{\infty} d\epsilon \frac{\Gamma^H_{\nu\tilde{m}}(\epsilon)}{\pi} f(\epsilon) e^{i\epsilon\tau} \\ &= G^<_{\nu,\tilde{m}}(\tau) = G^{<*}_{\nu,\tilde{m}}(-\tau), \end{aligned} \tag{B7a}$$

and the greater or hole GF,

$$\begin{aligned} G^>_{\nu,\tilde{m}}(t,t') &= -i|t'_{\nu\tilde{m}}|^2 \mathrm{Tr}_R[\rho_R c_{0\nu\tilde{m}}(t) c^\dagger_{0\nu\tilde{m}}(t')] \\ &= -i \int_{-\infty}^{\infty} d\epsilon \frac{\Gamma^H_{\nu\tilde{m}}(\epsilon)}{\pi} f(-\epsilon) e^{-i\epsilon\tau} \\ &= G^>_{\nu,\tilde{m}}(\tau) = G^{>*}_{\nu,\tilde{m}}(-\tau), \end{aligned} \tag{B7b}$$

only depend on the time difference $\tau = t - t'$ in equilibrium and fully determine the effect of the reservoirs onto the dynamics on the Wilson chain. Their Fourier transformations are defined as

$$G^{>(<)}(\omega) = \int_{-\infty}^{\infty} dt e^{-i\omega t} G^{>(<)}_{\nu,\tilde{m}}(t). \tag{B8}$$

The reduced density operator $\rho_S(t)$ obeys the time-local differential equation

$$\begin{aligned} \partial_t \rho_S(t) = &-i \sum_{\tilde{m}=0}^{N} \sum_{\nu} \int_0^t d\tau \rho_S(t) [f^\dagger_{\nu\tilde{m}}(t-\tau) f_{\nu\tilde{m}}(t) G^>_{\nu,\tilde{m}}(-\tau) - f_{\nu\tilde{m}}(t-\tau) f^\dagger_{\nu\tilde{m}}(t) G^<_{\nu,\tilde{m}}(-\tau)] \\ &+ i \sum_{\tilde{m}=0}^{N} \sum_{\nu} \int_0^t d\tau [f^\dagger_{\nu\tilde{m}}(t-\tau) \rho_S(t) f_{\nu\tilde{m}}(t) G^>_{\nu,\tilde{m}}(-\tau) - f_{\nu\tilde{m}}(t-\tau) \rho_S(t) f^\dagger_{\nu\tilde{m}}(t) G^<_{\nu,\tilde{m}}(-\tau)] \\ &+ i \sum_{\tilde{m}=0}^{N} \sum_{\nu} \int_0^t d\tau [f^\dagger_{\nu\tilde{m}}(t) \rho_S(t) f_{\nu\tilde{m}}(t-\tau) G^>_{\nu,\tilde{m}}(\tau) - f_{\nu\tilde{m}}(t) \rho_S(t) f^\dagger_{\nu\tilde{m}}(t-\tau) G^<_{\nu,\tilde{m}}(\tau)] \\ &- i \sum_{\tilde{m}=0}^{N} \sum_{\nu} \int_0^t d\tau [f^\dagger_{\nu\tilde{m}}(t) f_{\nu\tilde{m}}(t-\tau) G^>_{\nu,\tilde{m}}(\tau) - f_{\nu\tilde{m}}(t) f^\dagger_{\nu\tilde{m}}(t-\tau) G^<_{\nu,\tilde{m}}(\tau)] \rho_S(t) \end{aligned} \tag{B9}$$

after substituting the explicit form of $V_I(t)$ into Eq. (B6) and making use of the Markov approximation [24]: For fast decaying correlation functions $G^>_{\nu,m}(\tau)$, $G^<_{\nu,m}(\tau)$ relative to the change of $\rho_S(t)$, one can replace $\rho_S(t-\tau) \to \rho_S(t)$ under the integral, converting the integro-differential equation into a master equation for $\rho_S(t)$ and neglecting retardation effects. This approximation is the origin of the deviation between the analytical solution and the OC approach in Fig. 18 for very short times.

By calculating the trace on both sides of Eq. (B9), one obtains $\partial_t \mathrm{Tr}[\rho_S(t)] = 0$, since for each reservoir GF a pair of terms can be found which cancel each other out. Thus, the derived differential equation conserves the trace of the density operator at all times.

Conservation of the trace under the restriction $m_2 \in \{m_1 - 1, m_1, m_1 + 1\}$ (Eq. (52) has been used):

$$\sum_{m_1=m_{\min}}^{N} \sum_{l_1} \dot{\rho}^{\mathrm{red}}_{l_1,l_1}(m_1;t) = \sum_{m_1=m_{\min}}^{N} \sum_{m_2=m_1-1\geqslant m_{\min}}^{m_1+1\leqslant N} \sum_{l_1,l_2} \left(\Xi_{l_2,l_1}(m_2,m_1)\rho^{\mathrm{red}}_{l_2,l_2}(m_2;t) - \Xi_{l_1,l_2}(m_1,m_2)\rho^{\mathrm{red}}_{l_1,l_1}(m_1;t)\right). \tag{B10}$$

The two sums are interconvertible, so the trace is conserved.

APPENDIX C: ANALYTICAL SOLUTION TO SHORT-TIME DYNAMICS IN THE SIAM

When Eq. (B5) is integrated over time and then inserted into the time-dependent expectation value of any local operator O, we obtain

$$\langle O(t)\rangle = \mathrm{Tr}\{\rho_0 O^I(t)\} + \langle O'(t)\rangle, \quad \langle O'(t)\rangle \approx -\int_0^t d\tau_1 \int_0^{\tau_1} d\tau_2 \mathrm{Tr}\{\rho_0[H^I(\tau_2),[H^I(\tau_1),O^I(t)]]\} \tag{C1}$$

after replacing the full dynamics of the density operator by its initial values in the step from line one to line two. This is asymptotically exact for $t \to 0$ and defines a second-order approximation in the impurity bath coupling function. Here

$$H^I(\tau) = \sum_{k,\sigma} V_k (c^\dagger_{k\sigma}(\tau) d_\sigma(\tau) + c_{k\sigma}(\tau) d^\dagger_\sigma(\tau)) \tag{C2}$$

is the term for the interaction of the impurity level and the bath excitations. The operators in the interaction representation read

$$d_\sigma(t) = |0\rangle\langle\sigma| e^{-i\epsilon_d t} - \sigma |-\sigma\rangle\langle 2| e^{-i(\epsilon_d+U)t}, \tag{C3}$$

$$c_{k\sigma}(t) = c_{k\sigma} e^{-i\epsilon_k t}, \tag{C4}$$

where $|0\rangle$ is the vacuum state on the impurity, $|2\rangle$ the double occupied state, and $|\sigma\rangle$ accounts for either spin state $\uparrow$ or $\downarrow$. The density matrix ρ_0 factorizes for the interaction quench. We chose the parameter $E_d^0 = b_0/2 = \Gamma_0/2$ in the Hamiltonian Eq. (91) for $t < 0$.

Inserting Eq. (C2) into Eq. (C1) and evaluating the double commutators using the initial density matrix ρ_0, we obtain

$$\begin{aligned}\langle O'(t)\rangle = &\frac{2}{Z}\sum_{k,\sigma} V_k^2 A(\epsilon_k - \epsilon_d, t)\cdot[f(\epsilon_k)e^{-\beta E_0}(\langle\sigma\rangle - \langle 0\rangle) + f(-\epsilon_k)e^{-\beta E_\sigma}(\langle 0\rangle - \langle\sigma\rangle)] \\ &+ \frac{2}{Z}\sum_{k,\sigma} V_k^2 A(\epsilon_k - \epsilon_d - U, t)\cdot[f(\epsilon_k)e^{-\beta E_\sigma}(\langle 2\rangle - \langle\sigma\rangle) + f(-\epsilon_k)e^{-\beta E_2}(\langle\sigma\rangle - \langle 2\rangle)],\end{aligned} \tag{C5}$$

where we have used the shortcut notations $\langle s\rangle = \langle s|\, O\, |s\rangle$, $s \in \{0, \uparrow, \downarrow, 2\}$ and $A(\epsilon, t) = \frac{1-\cos(\epsilon t)}{\epsilon^2}$. For a constant hybridization function [see Eq. (35)] and applying the low-temperature limit, Eq. (C5) can be transformed to

$$O'(t) = (\langle\uparrow\rangle + \langle\downarrow\rangle - 2\langle 0\rangle)B_{-D,0}(t,\epsilon_d) + (\langle 0\rangle - \langle\uparrow\rangle)B_{0,D}(t,\epsilon_d) + (\langle 2\rangle - \langle\uparrow\rangle)B_{-D,0}(t,\epsilon_d + U). \tag{C6}$$

The integration can be done in an exact manner with

$$B_{a,b}(t,\epsilon') = \frac{\Gamma_0}{\pi}\int_a^b d\epsilon A(\epsilon - \epsilon', t) = \frac{\Gamma_0 t}{\pi}\mathrm{Si}((\epsilon - \epsilon')t) + \frac{\Gamma_0}{\epsilon - \epsilon'}\frac{\cos((\epsilon - \epsilon')t) - 1}{\pi}\Bigg|_{\epsilon=a}^{b}, \tag{C7}$$

where $\mathrm{Si}(\epsilon)$ is the sine integral.

For a nonconstant hybridization function $\Gamma(\epsilon)$, the integration can alternatively be performed by expanding the cosine functions as a series, obtaining

$$B_{a,b}(t,\epsilon') = \frac{b-a}{2}t^2 + \sum_{n=2}^{\infty}\frac{(b-\epsilon')^{2n-1} - (a-\epsilon')^{2n-1}}{(-1)^{n-1}(2n)!(2n-1)}t^{2n} \tag{C8}$$

for the constant case. Assuming the symmetric SIAM by choosing $\epsilon_d = E_d^1 = -U/2$ and exploiting the fact that $B_{-D,0}(t,\epsilon) = B_{0,D}(t,-\epsilon)$, we arrive at the final result of Eq. (C1):

$$n_\uparrow(t) = \tfrac{1}{2} + B_{0,D}(t, U/2) - B_{0,D}(t, -U/2), \quad n_\downarrow(t) = B_{0,D}(t, U/2) + B_{0,D}(t, -U/2), \tag{C9}$$

$$n_d(t) = n_\uparrow(t) + n_\downarrow(t) = \tfrac{1}{2} + 2B_{0,D}(t, U/2), \quad S_z(t) = \tfrac{1}{2}(n_\uparrow(t) - n_\downarrow(t)) = \tfrac{1}{4} - B_{0,D}(t, -U/2). \tag{C10}$$

[1] M. A. Kastner, Rev. Mod. Phys. **64**, 849 (1992).

[2] D. Goldhaber-Gordon, H. Shtrikman, D. Mahalu, D. Abusch-Magder, U. Meirav, and M. Kastner, Nature **391**, 156 (1998).

[3] D. Goldhaber-Gordon, J. Göres, M. A. Kastner, H. Shtrikman, D. Mahalu, and U. Meirav, Phys. Rev. Lett. **81**, 5225 (1998).

[4] W. G. van der Wiel, S. D. Franceschi, T. F. J. Elzerman, S. Tarucha, and L. P. Kouvenhoven, Science **289**, 2105 (2000).

[5] H. C. Manoharan, C. P. Lutz, and D. M. Eigler, Nature **403**, 512 (2000).
[6] O. Agam and A. Schiller, Phys. Rev. Lett. **86**, 484 (2001).
[7] R. Temirov, A. Lassise, F. B. Anders, and F. S. Tautz, Nanotechnology **19**, 065401 (2008).
[8] M. Galperin, A. Nitzan, and M. A. Ratner, Phys. Rev. Lett. **96**, 166803 (2006).
[9] J. R. Heath, Annu. Rev. Mater. Res. **39**, 1 (2009).
[10] N. Lorente and M. Persson, Phys. Rev. Lett. **85**, 2997 (2000).
[11] M. A. Reed, Mater. Today **11**, 46 (2008).
[12] F. Eickhoff, E. Kolodzeiski, T. Esat, N. Fournier, C. Wagner, T. Deilmann, R. Temirov, M. Rohlfing, F. S. Tautz, and F. B. Anders, Phys. Rev. B **101**, 125405 (2020).
[13] V. M. Pereira, F. Guinea, J. M. B. L. dos Santos, N. M. R. Peres, and A. H. C. Neto, Phys. Rev. Lett. **96**, 036801 (2006).
[14] M. A. Cazalilla, A. Iucci, F. Guinea, and A. H. C. Neto, arXiv:1207.3135.
[15] D. May, P.-W. Lo, K. Deltenre, A. Henke, J. Mao, Y. Jiang, G. Li, E. Y. Andrei, G.-Y. Guo, and F. B. Anders, Phys. Rev. B **97**, 155419 (2018).
[16] Y. Jiang, P.-W. Lo, D. May, G. Li, G.-Y. Guo, F. B. Anders, T. Taniguchi, K. Watanabe, J. Mao, and E. Y. Andrei, Nat. Commun. **9**, 2349 (2018).
[17] Y. Kuramoto, in *Theory of Heavy Fermions and Valence Fluctuations*, edited by T. Kasuya and T. Saso (Springer Verlag, Berlin, 1985), p. 152.
[18] A. Georges, G. Kotliar, W. Krauth, and M. J. Rozenberg, Rev. Mod. Phys. **68**, 13 (1996).
[19] G. Kotliar and D. Vollhardt, Phys. Today **57**(3), 53 (2004).
[20] J. M. Elzerman, R. Hanson, L. H. W. van Beveeren, B. Witkamp, L. M. K. Vandersypen, and L. P. Kouvenhoven, Nature **430**, 431 (2004).
[21] R. Hanson, L. P. Kouwenhoven, J. R. Petta, S. Tarucha, and L. M. K. Vandersypen, Rev. Mod. Phys. **79**, 1217 (2007).
[22] A. J. Leggett, S. Chakravarty, A. T. Dorsey, and M. P. A. Fisher, Rev. Mod. Phys. **59**, 1 (1987).
[23] B. Bertini, F. Heidrich-Meisner, C. Karrasch, T. P. nd R. Steinigeweg, and M. Znidaric, arXiv:2003.03334.
[24] V. May and O. Kühn, *Charge and Energy Transfer Dynamics in Molecular Systems* (Wiley-VCH, Berlin, 2000).
[25] L. V. Keldysh, Sov. Phys. JETP **20**, 1018 (1965).
[26] L. P. Kadanoff and G. Baym, *Quantum Statistical Mechanics* (Benjamin, New York, 1962).
[27] D. C. Langreth and J. W. Wilkins, Phys. Rev. B **6**, 3189 (1972).
[28] A.-P. Jauho, N. S. Wingreen, and Y. Meir, Phys. Rev. B **50**, 5528 (1994).
[29] P. Nordlander, M. Pustilnik, Y. Meir, N. S. Wingreen, and D. C. Langreth, Phys. Rev. Lett. **83**, 808 (1999).
[30] D. M. Kennes, S. G. Jakobs, C. Karrasch,, and V. Meden, Phys. Rev. B **85**, 085113 (2012).
[31] C. Karrasch, S. Andergassen, M. Pletyukhov, D. Schuricht, a. V. M. L. Borda, and H. Schoeller, Europhys. Lett. **90**, 30003 (2010).
[32] H. Schoeller, Eur. Phys. J.: Spec. Top. **168**, 179 (2009).
[33] F. Wegner, Ann. Phys. **506**, 77 (1994).
[34] S. Kehrein, Phys. Rev. Lett. **95**, 056602 (2005).
[35] E. Gull, A. J. Millis, A. I. Lichtenstein, A. N. Rubtsov, M. Troyer, and P. Werner, Rev. Mod. Phys. **83**, 349 (2011).
[36] L. Mühlbacher and E. Rabani, Phys. Rev. Lett. **100**, 176403 (2008).
[37] T. L. Schmidt, P. Werner, L. Mühlbacher, and A. Komnik, Phys. Rev. B **78**, 235110 (2008).
[38] M. Schiró, Phys. Rev. B **81**, 085126 (2010).
[39] G. Cohen, E. Gull, D. R. Reichman, and A. J. Millis, Phys. Rev. Lett. **115**, 266802 (2015).
[40] H. J. Carmichael, *Statistical Methods in Quantum Optics 1* (Springer Verlag, Berlin, 1999).
[41] M. Nuss, G. Dorn, A. Dorda, W. von der Linden, and E. Arrigoni, Phys. Rev. B **92**, 125128 (2015).
[42] A. Dorda, M. Ganahl, H. G. Evertz, W. von der Linden, and E. Arrigoni, Phys. Rev. B **92**, 125145 (2015).
[43] A. B. J. Kuijlaars, SIAM J. Matrix Anal. Appl. **22**, 306 (2000).
[44] Y. Saad, *Iterative Methods for Sparse Linear Systems* (Society for Industrial and Applied Mathematics, 2003).
[45] H. Tal-Ezer and R. Kosloff, J. Chem. Phys. **81**, 3967 (1984).
[46] R. Kosloff, Annu. Rev. Phys. Chem. **45**, 145 (1994).
[47] A. Weiße, G. Wellein, A. Alvermann, and H. Fehske, Rev. Mod. Phys. **78**, 275 (2006).
[48] R. Steinigeweg, J. Gemmer, and W. Brenig, Phys. Rev. Lett. **112**, 120601 (2014).
[49] J. Hackmann and F. B. Anders, Phys. Rev. B **89**, 045317 (2014).
[50] F. B. Anders and A. Schiller, Phys. Rev. Lett. **95**, 196801 (2005).
[51] F. B. Anders and A. Schiller, Phys. Rev. B **74**, 245113 (2006).
[52] F. B. Anders, Phys. Rev. Lett. **101**, 066804 (2008).
[53] H. T. M. Nghiem and T. A. Costi, Phys. Rev. B **89**, 075118 (2014).
[54] H. T. M. Nghiem and T. A. Costi, Phys. Rev. Lett. **119**, 156601 (2017).
[55] A. J. Daley, C. Kollath, U. Schollwöck, and G. Vidal, J. Stat. Mech.: Theor. Exp. (2004) P04005.
[56] U. Schollwöck, Rev. Mod. Phys. **77**, 259 (2005).
[57] U. Schollwöck, Ann. Phys. (Amsterdam) **326**, 96 (2011).
[58] R. Bulla, T. A. Costi, and T. Pruschke, Rev. Mod. Phys. **80**, 395 (2008).
[59] E. Eidelstein, A. Schiller, F. Güttge, and F. B. Anders, Phys. Rev. B **85**, 075118 (2012).
[60] F. Güttge, F. B. Anders, U. Schollwoeck, E. Eidelstein, and A. Schiller, Phys. Rev. B **87**, 115115 (2013).
[61] G. Schneider and P. Schmitteckert, arXiv:cond-mat/0601389.
[62] B. Bruognolo, N.-O. Linden, F. Schwarz, S.-S. B. Lee, K. Stadler, A. Weichselbaum, M. Vojta, F. B. Anders, and J. von Delft, Phys. Rev. B **95**, 121115(R) (2017).
[63] R. Bulla, N.-H. Tong, and M. Vojta, Phys. Rev. Lett. **91**, 170601 (2003).
[64] K. G. Wilson, Rev. Mod. Phys. **47**, 773 (1975).
[65] H. R. Krishna-murthy, J. W. Wilkins, and K. G. Wilson, Phys. Rev. B **21**, 1003 (1980).
[66] P. W. Vigman and A. M. Finkelstein, Zh. Eksp. Theor. Fiz. **75**, 204 (1978) [Sov. Phys. JETP **48**, 102 (1978)].
[67] P. Schlottmann, Phys. Rev. B **22**, 613 (1980).
[68] R. Bulla, T. Pruschke, and A. C. Hewson, J. Phys.: Condens. Matter **9**, 10463 (1997).
[69] M. Vojta, N.-H. Tong, and R. Bulla, Phys. Rev. Lett. **102**, 249904(E) (2009).
[70] M. Vojta, R. Bulla, F. Güttge, and F. Anders, Phys. Rev. B **81**, 075122 (2010).

[71] S. White, Phys. Rev. Lett. **69**, 2863 (1992).
[72] C. Grenzebach, F. B. Anders, G. Czycholl, and T. Pruschke, Phys. Rev. B **74**, 195119 (2006).
[73] C. Grenzebach, F. B. Anders, G. Czycholl, and T. Pruschke, Phys. Rev. B **77**, 115125 (2008).
[74] M. Karski, C. Raas, and G. S. Uhrig, Phys. Rev. B **77**, 075116 (2008).
[75] S. Schmitt and F. B. Anders, Phys. Rev. B **81**, 165106 (2010); Phys. Rev. Lett. **107**, 056801 (2011).
[76] A. Jovchev and F. B. Anders, Phys. Rev. B **87**, 195112 (2013).
[77] Y. Meir and N. S. Wingreen, Phys. Rev. Lett. **68**, 2512 (1992).
[78] S. Hershfield, Phys. Rev. Lett. **70**, 2134 (1993).
[79] F. Güttge, Ph.D. thesis, Department of Physics, Technical University Dortmund, 2013.
[80] J. M. Deutsch, Phys. Rev. A **43**, 2046 (1991).
[81] M. Srednicki, Phys. Rev. E **50**, 888 (1994).
[82] M. Rigol, V. Dunjko, and M. Olshanii, Nature **452**, 854 (2008).
[83] M. Rigol and M. Srednicki, Phys. Rev. Lett. **108**, 110601 (2012).
[84] A. Weichselbaum and J. von Delft, Phys. Rev. Lett. **99**, 076402 (2007).
[85] A. A. Dzhioev and D. S. Kosov, J. Phys.: Condens. Matter **24**, 225304 (2012).
[86] M. Yoshida, M. A. Whitaker, and L. N. Oliveira, Phys. Rev. B **41**, 9403 (1990).
[87] P. Schmitteckert, J. Phys.: Conf. Ser. **220**, 012022 (2010).
[88] P. Schlottmann, J. Magn. Magn. Mater. **7**, 72 (1978).
[89] P. Mehta and N. Andrei, Phys. Rev. Lett. **96**, 216802 (2006).
[90] E. Boulat, H. Saleur, and P. Schmitteckert, Phys. Rev. Lett. **101**, 140601 (2008).
[91] G. Barcza, K. Bauerbach, F. Eickhoff, F. B. Anders, F. Gebhard, and O. Legeza, Phys. Rev. B **101**, 075132 (2020).
[92] H. Haug and S. W. Koch, *Quantum Theory of the optical and Electronic Properties of Semiconductors* (World Scientific, Singapore, 2004).